PCCP

Electric double layer structure and differential capacitance at the electrode interface of tributylmethylammonium bis(trifluoromethanesulfonyl)amide studied using molecular dynamics simulation.

Journal:	*Physical Chemistry Chemical Physics*
Manuscript ID	CP-ART-09-2019-005297.R2
Article Type:	Paper
Date Submitted by the Author:	n/a
Complete List of Authors:	Katakura, Seiji; Kyoto University, Department of Energy and Hydrocarobon Chemistry Nishi, Naoya; Kyoto Univ., Graduate School of Engineering Kobayashi, Kazuya; Kyoto University Amano, Ken-ichi; Kyoto University, Department of Energy and Hydrocarbon Chemistry; Meijo University, Facluty of Agriculture Sakka, Tetsuo; Kyoto University, Department of Energy and Hydrocarbon Chemistry

SCHOLARONE™
Manuscripts

PCCP

Physical Chemistry Chemical Physics

Guidelines for Reviewers

Thank you very much for agreeing to review this manuscript for *Physical Chemistry Chemical Physics (PCCP)*.

PCCP is an international journal for the publication of cutting-edge original work in physical chemistry, chemical physics and biophysical chemistry. To be suitable for publication in *PCCP*, articles must include significant innovation and/or insight into physical chemistry; this is the most important criterion that reviewers and the Editors will judge against when evaluating submissions. Further information on our scope can be found at rsc.li/pccp.

PCCP's Impact Factor is **3.567** (2018 Journal Citation Reports®)

The following manuscript has been submitted for consideration as a

PAPER

Full papers should contain original scientific work that has not been published previously. Full papers based on Communications are encouraged provided that they represent a substantial extension of the original material. There are no restrictions on the length of a paper. Authors should include a brief discussion in the Introduction that sets the context for the new work and gives their motivation for carrying out the study.

When preparing your report, please:

- Focus on the originality, importance, impact and reliability of the science. English language and grammatical errors do not need to be discussed in detail, except where it impedes scientific understanding.
- Use the journal scope and expectations to assess the manuscript's suitability for publication in *PCCP.*
- State clearly whether you think the article should be accepted or rejected and include details of how the science presented in the article corresponds to publication criteria.
- Inform the Editor if there is a conflict of interest, a significant part of the work you cannot review with confidence or if parts of the work have previously been published.

Best regards,

Professor David Rueda
Editorial Board Chair
Imperial College London, UK

Dr Anna Simpson
Executive Editor
Royal Society of Chemistry

Contact us

Please visit our reviewer hub for further details of our processes, policies and reviewer responsibilities as well as guidance on how to review, or click the links below.

What to do when you review

Reviewer responsibilities

Process & policies

PCCP

ARTICLE TYPE

Cite this: DOI: 00.0000/xxxxxxxxxx

Electric double layer structure and differential capacitance at the electrode interface of tributylmethylammonium bis(trifluoromethanesulfonyl)amide studied using molecular dynamics simulation.†

Seiji Katakura,[a] Naoya Nishi,*[a] Kazuya Kobayashi,[a] Ken-ichi Amano[a,b] and Tetsuo Sakka[a]

Received Date
Accepted Date

DOI: 00.0000/xxxxxxxxxx

A molecular dynamics simulation at the electrode interface of a quaternary ammonium ionic liquid, tributylmethylammonium bis(trifluoromethanesulfonyl)amide ($[N^+_{1444}][TFSA^-]$), has been performed. Unlike the commonly used cations, such as 1-alkyl-3-methylimidazolium and 1,1-alkylmethylpyrrolidinium cations, N^+_{1444} has multiple long-alkyl groups (three butyl groups). The behavior of ions at the electrode interface, especially these butyl groups has been investigated. N^+_{1444} at the first layer mainly has two types of orientations, lying and standing. The lying orientation is dominant at moderately negative potentials. However, the standing one becomes dominant at the more negative potentials. Due to this orientational change, the number of N^+_{1444} increases at the first layer as the potential becomes negative even at the potentials where the anions are completely depleted there. The change in orientation results in the upward deviation of the differential capacitance from the theoretical prediction at the negative potentials. The results suggest that the orientational preference caused by the steric constraint between alkyl groups plays an important role in the behavior of the electric double layer of the ionic liquids.

1 Introduction

Ionic liquids (ILs) are low-melting point salts that are only composed of ions. ILs have a wide potential window, high thermal stability, moderate ionic conductivity, and non-flammability. Since these properties are desirable to electrochemical materials, ILs have been applied to Li-ion batteries,[1] electric double layer capacitors,[2] fuel cells,[3] and many other electrochemical systems.[4] In these applications, chemical reactions and mass transfer at the interface between ILs and electrodes often play an important role. Hence, it is necessary to clarify the electric double layer (EDL) structure of ILs to understand and control these phenomena.

The EDL structure of ILs has been proposed to be unique due to excluded volume and local electrostatic interactions between ions.[5] In the case of dilute electrolyte solutions, conventional models such as the Gouy-Chapman model[6,7] can elucidate the EDL structure, without taking into account such interactions. However, the assumption of dilute solution is obviously inadequate for ILs because ILs themselves are solute ions and solvents. Kornyshev has proposed an EDL model for ILs[5] using a lattice gas model with mean-field approximation, which considers the excluded volume effect of ions as a local electrostatic interaction. Kornyshev's model predicts the potential dependence of the differential capacitance (C_d) for EDL of ILs. The predicted potential-C_d curve has a bell or camel shape depending on constituent ions: The bell shape curve has a maximum at the potential of zero charges (PZC), and the camel shape curve has two maxima at positive and negative potential sides of PZC. Recently, improved lattice gas models have also been proposed which consider the asymmetry of the ion size[8,9] and local electrostatic interaction between ions.[10,11] Molecular dynamics (MD) simulation studies[12–15] using all-atom models, which involves the geometric effect of the ions, have confirmed the camel and bell shape on the potential-C_d curve. Experimentally, the electrochemical impedance spectroscopy measurements[16–19] have also reported such behaviors. We have studied static (zero frequency) C_d using the pendant drop method,[20–22] which can avoid hysteresis[17,22–25] and the effect of slow relaxation[18,26–28] of the EDL structure, and succeeded in quantitatively analyzing the experimental potential-C_d curves with the lattice gas models.

[a] Address, Department of Energy and Hydrocarbon Chemistry, Graduate School of Engineering, Kyoto University, Kyoto 615-8510, Japan. Fax: 075 383 2490; Tel: 075 383 2491; E-mail: nishi.naoya.7e@kyoto-u.ac.jp
[b] Address, Faculty of Agriculture, Meijo University, Nagoya, Aichi 468-8502, Japan.

† Electronic Supplementary Information (ESI) available: [details of any supplementary information available should be included here]. See DOI: 10.1039/cXCP00000x/

The EDL characteristics of ILs have been revealed not only from macroscopic quantities such as C_d but also from the microscopic structure like the distribution and orientation of ions by using X-ray reflectometry (XR),[28–33] neutron reflectometry (NR),[34,35] atomic force microscope (AFM),[36,37] surface force apparatus (SFA),[38] scanning tunneling microscope (STM)[37,39] sum frequency generation (SFG),[40,41] surface enhanced infrared absorption spectroscopy (SEIRAS),[23,24] surface-enhanced Raman scattering (SERS),[42,43] and MD simulation.[12,15,44–49]

Quaternary ammonium-based ILs (QaILs) have a particularly wide potential window and therefore are desirable as electrolytes. Also, since a Qa cation has multiple alkyl groups, QaILs have more freedom in designing the ionic structure than imidazolium-based ILs. The EDL structure of QaILs has been rarely reported in contrary to the fact that many studies have been reported for the EDL structure of imidazolium-based ILs. Sharma and Kashyap[47] studied the EDL structure at the interface between QaILs and graphene electrode using triethyloctylammonium and (2-ethoxyethoxy)ethyltriethylammonium as constituent cations and bis(trifluoromethansulfonyl)amide ($TFSA^-$) as the common anion using MD simulation. Substituting alkyl group with diether group, the authors found the change in the EDL structure, such as an increase in the parallel orientation of the longest tail near the electrode for the diether one compared to the alkyl one. They also studied EDL structure and the electrostatic properties of pyrrolidinium-based ILs, which have quaternary ammonium and cyclic structure, with focusing on the role of linear and nonlinear alkyl tails.[48,49] We have previously studied the EDL structure at the interface between QaILs and gold electrode using SEIRAS[50] and elucidated that the behavior of Qa cations in the EDL is affected not only by the length of alkyl chain in Qa cations but also by that of the perfluoroalkyl chain in the anion. Moreover, we have studied the dynamics of the EDL structure of QaILs using electrochemical surface plasmon resonance (ESPR)[27,51] and revealed the ultra-slow dynamics on the order of minutes. We also investigated the surface structure of QaILs by using XR[52,53] and found the spontaneous formation of ionic multilayers. We performed MD at the interface between QaILs and vacuum[54] and clarified the effect of the number of long alkyl chains in Qa cation on the interfacial structure. Nevertheless, the EDL structure of QaILs is hardly elucidated at present, and therefore, the potential dependence of orientations and distributions of ions should be clarified.

In the present study, we studied the EDL structure of tributylmethylammonium $TFSA^-$ ($[N^+_{1444}][TFSA^-]$) at the molecular level by using MD simulation. N^+_{1444} has a three-dimensional structure in which three butyl groups surround the polar part. Since such bulky non-polar parts lead to complicated steric constraint between neighboring cations in EDL, they play an important role in the EDL structure. Therefore, we evaluated the EDL structure by focusing on the behavior of both the polar parts and butyl chains at the first layer.

2 Methods

2.1 Computational detail

MD simulation at the interface of $[N^+_{1444}][TFSA^-]$ | graphene electrode was performed using DL_POLY classic.[55] The structure of $[N^+_{1444}][TFSA^-]$ and the definitions of atomic names are shown in Fig. 1.

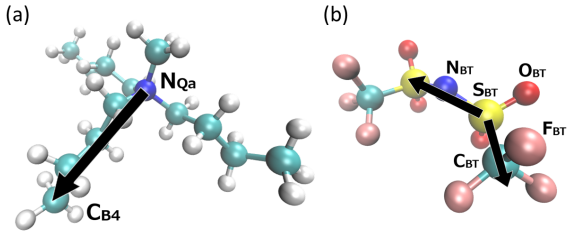

Fig. 1 Structure of (a) N^+_{1444} and (b) $TFSA^-$, and definitions of intramolecular vector to calculate the orientations of ions. N_{Qa} and N_{BT} are assumed as a representative of polar-part of N^+_{1444} and $TFSA^-$. C_{B4} is assumed as that of nonpolar-part of N^+_{1444}.

We used an all-atom force field, CL&P,[56] for $[N^+_{1444}][TFSA^-]$. The specific parameters are described elsewhere.[54] For the force field of the graphene carbon atoms, we used the van der Walls parameter of the sp_2 carbon atom from OPLS AA.[57] We set the surface charge density of the graphene σ_{elec} by evenly allocating the charge to each carbon atom constituting graphene. The cutoff distance of the vdW force was 10 Å. For the calculation of long-range force, three-dimensional smooth particle mesh Ewald method[58] (SPME) was used with an accuracy of 10^{-5}, and the real space cutoff was set to 10 Å. In order to take electronic polarization into account,[59,60] the electrostatic interaction was scaled with relative permittivity $\varepsilon_r = 2$.[54,61] No slab correction for 3-dimensional periodicity was used. Although it is desirable to include slab correction, the presence or absence of slab correction did not cause any serious problem on the discussion made in the present study. We examined the effect of the correction and found that the interfacial potential difference in the present study was lower than that with the correction (see Fig. S3). This is consistent with a previous MD study[15] that compared the effect of slab correction.

The same initial configuration of the interface between $[N^+_{1444}][TFSA^-]$ and graphene was used for all the charged conditions. The initial configuration was made through bulk simulation, vacuum|liquid interface simulation, and equilibrated by uncharged graphene interface simulation. The numbers of ion pairs in the system were 180, 360, and 360, respectively. The procedure of bulk simulation and vacuum|liquid Maninterface simulation was described elsewhere.[54] Orthorhombic MD cells (Fig. 2), were used for the interface simulations with geometries (l_x, l_y, l_z), where l_x, l_y, and l_z are the side lengths in x-, y-, and z-direction, respectively. The cell has a ~100 Å thick IL slab confined by electrodes and ~200 Å thick vacuum. The l_x and l_y ($l_x = l_y = 49.9635$ Å) of the equilibrium configuration of the gas-liquid interface were slightly expanded to (l_x, l_y) = (51.6852 Å, 51.1560 Å), which correspond to an integral multiple of the unit

cell of graphene sheet. Then two graphene sheets were put at the vacuum phase near the interfaces at the positive side and negative side of z. Then the positions of the graphene sheets were adjusted and fixed so that the cavity between the sheet and IL disappeared. Even after the disappearance of cavities, the IL density is low. Hence, the configuration was compressed in the z-direction so that the further calculation gives the same density at the IL bulk region as the vacuum-liquid interface MD in our previous study[54](see Fig. S1). In the compressed configuration, the distance between the two graphene electrodes was 103.1 Å. From this configuration, a calculation was performed for 3 ns to obtain the configuration which is used as a common initial configuration for different σ_{elec}.

Starting from this initial configuration, a set of electrode interface MD calculations was performed by changing σ_{elec}. Charges were equally distributed to the each carbon atom of electrode to give $\pm$ σ_{elec} for each electrode. Then 3 ns calculation was performed. The first 1 ns was regarded as an equilibration process, and the remaining 2 ns was used for data analysis. The geometry of this MD cell was (l_x, l_y, l_z) = (51.6852 Å, 51.1560 Å, 300.0000 Å) (See Fig. 2). The $|\sigma_{\mathrm{elec}}|$values were varied as a minimum unit with 1.01 μC/cm^2 in the range from 0 to 12.11 μC/cm^2, and 3.03 μC/cm^2 in the range from 12.11 to 36.36 μC/cm^2. The MD simulation was performed in the NVT ensemble. The time step was 2 fs in all cases. The temperature was controlled at 423 K using a Berendsen thermostat.[62] Although the Berendsen thermostat may cause artificial collective motion[63] in some simulation systems and therefore the use of other thermostats[64–66] is preferred, we did not observe such an artificial motion of ions.

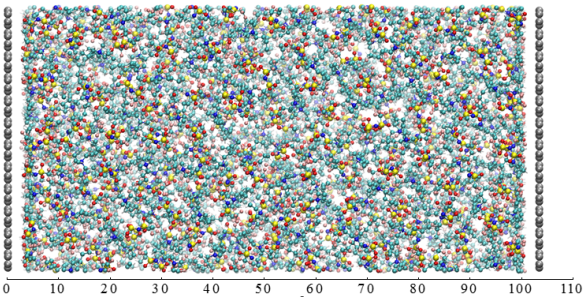

Fig. 2 Geometry of the MD cell.

2.2 Data analysis

MD trajectories were analyzed to produce number density distributions $\rho_{\mathrm{i}}(z)$ for each atom i as a function of z, the distance from the electrode (the center of the graphene C atom). We regarded the N atoms of N^+_{1444} and $TFSA^-$ (N_{Qa} and N_{BT} respectively, see Fig. 1) as representative points of the polar part of each ion, and C atoms at the end of the butyl chains (C_{B4}) as those of non-polar part. To investigate changes in the composition of the first layer at the interface, we calculated surface densities Γ of atoms i there (i = N_{Qa}, N_{BT}, and C_{B4}) by integrating the first peak of the number density distributions as follows.

$$\Gamma_{\mathrm{i}} = \int_0^{z_{\mathrm{div}}} \rho_{\mathrm{i}} \mathrm{d}z \tag{1}$$

The upper limit of the integration (z_{div}) for N_{Qa}, N_{BT}, and C_{B4} were set to be 6.55, 6.45, and 6.95 Å, respectively, which were determined to cover the first peak of ρ_{i} for all σ_{elec} conditions.

The orientational distributions $p_{\mathrm{i\text{-}j}}(\theta)$ of the intramolecular vectors from atom i to j (i-j = N_{Qa}-C_{B4}, S_{BT}-S_{BT} and S_{BT}-C_{BT}, see Fig. 1 for the definitions) in the first layer were calculated. $p_{\mathrm{i\text{-}j}}(\theta)$ is defined so that it satisfies

$$\int_0^{2\pi}\int_0^{\pi} p_{\mathrm{i\text{-}j}}(\theta,\psi)\sin\theta \mathrm{d}\theta\mathrm{d}\psi = 4\pi. \tag{2}$$

Here, θ is the angle between the intramolecular vector and the z axis, i.e. polar angle, and ψ is the azimuthal angle. Since the assumption that $p_{\mathrm{i\text{-}j}}(\theta,\ \psi)$ does not depend on ψ is reasonable (see Fig. S2), the eq. (2) can be integrated over ψ, as follows,

$$\int_0^{\pi} p_{\mathrm{i\text{-}j}}(\theta)\sin\theta \mathrm{d}\theta = 2 \tag{3}$$

If an intramolecular vector have an isotopic distribution as in bulk, then $p_{\mathrm{i\text{-}j}}(\theta) = 1$ for any value of θ. Note that $p(\theta)$ is not a population distribution function but a probability density function. To determine if an ion is at the first layer, the z position of N atom of N^+_{1444} and $TFSA^-$ (N_{Qa} and N_{BT}) was compared with z_{div}. Therefore, one can obtain the population of the vector i-j at θ by multiplying $p(\theta)$ with $\sin\theta$, which is the contribution of solid angle, and Γ_{i}. Because of the structure of the ions, three different intramolecular vectors of N_{Qa}-C_{B4} can be defined for each ion. Their three θ were calculated independently, and then averaged as $p_{\mathrm{i\text{-}j}}(\theta)$. Two different intramolecular vectors of S_{BT}-S_{BT}, and S_{BT}-C_{BT} were treated in the same way.

In order to investigate the in-plane structure of the first layer, the two-dimensional radial distribution functions for N_{Qa}-N_{Qa} and N_{BT}-N_{BT} in the layer were calculated. Here, the two-dimensional radial distribution function $g_{xy,\mathrm{i}}$ is expressed by the following equation.

$$g_{xy,\mathrm{i}}(r_{xy}) = \frac{\Delta n_{\mathrm{i}}(r_{xy})}{2\pi r \Delta r_{xy}\rho_{\mathrm{surf}}} \tag{4}$$

where, r_{xy} is the projected distance between two i atoms onto the xy plane, and $\Delta n_{\mathrm{i}}(r_{xy})$ is the number of atoms i present from r_{xy} to $r_{xy}+\Delta r_{xy}$, and ρ_{surf} is the surface density of atom i in the first layer.

Charge density distribution $\rho_{\mathrm{chg}}(z) = \sum_i \rho_{\mathrm{i}}(z)q_{\mathrm{i}}$, where q_{i} is a partial charge of the atom i, was calculated and converted into the potential distribution profile $\phi(z)$ (See Fig. S4) using the Poisson equation. The one-dimensional Poisson equation is as follows

$$\frac{\mathrm{d}^2}{\mathrm{d}z^2}\phi = -\frac{\rho_{\mathrm{chg}}}{\varepsilon_0\varepsilon_{\mathrm{r}}} \tag{5}$$

where ε_0 is the dielectric constant of vacuum and ε_{r} = 2 is the relative permittivity. Since SPME was used without using a slab correction, the "tin foil boundary condition" has been established, which means the potentials at both sides of periodic boundaries for each direction of the MD cell should be the same. There-

fore, the first integral constant for the Poisson equation was determined to satisfy the condition for the boundary in z-direction. The second integration constant was determined to set the potential in the IL bulk (ϕ_{bulk}) to be 0. Here, ϕ_{bulk} was obtained by averaging the electric potential in the range of ± 20 Å from the middle (z_{cent}) of the z coordinate of the two electrodes. Since $\phi_{\mathrm{bulk}} = 0$, the potential at the electrode ($z = 0$) represents the interfacial potential difference ($\Delta\phi = \phi_{\mathrm{elec}} - \phi_{\mathrm{bulk}}$).

The differential capacitance C_{d} for each potential were calculated by numerically differentiating the surface charge density σ_{elec} of the electrode with respect to $\Delta\phi$ as shown in the following formula.

$$C_{\mathrm{d}} = \frac{\mathrm{d}\sigma_{\mathrm{elec}}}{\mathrm{d}\Delta\phi} \tag{6}$$

For the numerical differentiation of eq. (6), quadratic regression was applied for each five consecutive points in the σ_{elec}-$\Delta\phi$ plot shown in Fig. S3. Four consecutive points were used for the second potential from the edge (-8.3 V and 5.1 V) in Fig. S3.

3 Results and Discussions

3.1 Number density distributions

The number density distributions as a function of the distance from the electrode (z) are shown in Fig. 3 (a)-(e), for N atom in N^+_{1444} (N_{Qa}), and C atoms at the end of butyl groups in N^+_{1444} (C_{B4}), and N atom in $TFSA^-$ (N_{BT}). All of these number density distributions showed oscillation which attenuated from the interface to the bulk. The oscillation of the N_{Qa} and N_{BT} were almost in phase when the electrode was not charged (Fig. 3 (c)), but were out of phase when the electrode was charged (Fig. 3 (a), (b), (d), and (e)). When the electrode is positively charged (Fig. 3 (a) and (b)), the odd- and even-number-th layers were composed of $TFSA^-$ and N^+_{1444}, respectively, and the order was reversed when the electrode was negatively charged. These results are consistent with previous studies by XR[25,29] and MD[25,44] for other types of ILs and an MD study for QaILs.[47] These results at relatively less charged interface also consistent with our previous studies[67,68] using integral equation theory.

To understand the gradual change in number density distributions at different potentials, their contour maps are also shown in Fig. 3 (f), (g), and (h) for N_{Qa}, N_{BT}, C_{B4}, respectively, with being normalized by the bulk density. All of these number density distributions at any potentials showed particularly sharp peaks either or both at $z \sim 4$ and ~ 8 Å, corresponding to the first and second layer, respectively. Since the peak at $z \sim 4$ Å for these atoms did not show large shift, we were able to define the boundary between the layers (z_{div}) for N_{Qa}, C_{B4}, N_{BT} as 6.55, 6.45, 6.95 Å, respectively. The boundaries are shown as the vertical dotted lines in Fig. 3 (f), (g), and (h). These values were determined to cover the first peak for all σ_{elec} conditions as described in the data analysis section.

First, we focus on the amplitude of the oscillation of N_{Qa} and N_{BT} (Fig. 3 (f) and (g)). As already shown in Fig. 3 (a) and (b), N_{Qa} forms the second ionic layer ($z \sim 8$ Å) at positive potentials, while N_{BT} forms the first ionic layer ($z \sim 4$ Å). It was reversed on the negative potentials. The peaks at $z \sim 8$ Å for N_{BT} and at $z \sim 13$ Å for N_{Qa} were highest at -2 V, which means alternating cation and anion layers are predominant at the potential, as exemplified in Fig. 3 (d). When the potential became more negative than -2 V, the amplitude of the oscillation decreased. The oscillation in Fig. 3 (f) and (g) becomes the smallest on the negative potentials at -5.4 V, which corresponds to Fig. 3 (e). In Fig. 3 (e), the number density distribution of N_{Qa} atoms showed a small peak in the second layer ($z \sim 8$ Å) next to the big first layer peak, indicating the negative charge on the electrode beyond the limit of charge compensation by the first ionic layer. In other words, the first layer is saturated with cations. The development of second ionic layer by the cation at the more negative potentials in Fig. 3 (f) is a result of the saturation.

Such saturation is called "crowding" and has been revealed by MD[44,69] and theory[70] for the EDL in ILs. The present result in negative potentials agrees with the previous MD studies.[44,69] In the positive potentials, the "crowding" of $TFSA^-$ was not observed because the potentials are not positive enough. According to one of the previous studies,[69] the crowding is accomplished by the larger surface charge density of the electrode for the smaller IL ions. We compared the molecular volumes of N^+_{1444} and $TFSA^-$ from DFT calculations at B3LYP/6-311++G(d,p) level using Gaussian 09W.[71] The volume of $TFSA^-$ (128 cm^3 mol^{-1}) was smaller than that of N^+_{1444} (205 cm^3 mol^{-1}). The small size of $TFSA^-$ will be the reason why the crowding of $TFSA^-$ was not observed within the σ_{elec} (potential) range studied.

Next, we focus on peak shifts depending on the potential in Fig. 3 (f) and (g). In Fig. 3 (f), the first ionic layer of N_{Qa} ($z \sim 4$ Å) showed peak shift only slightly, which implies that the orientation change of N^+_{1444} has little effect on the distance of the polar part of N^+_{1444} from the electrode. Conversely, in Fig. 3 (g), the first ionic layer of N_{BT} shifted particularly at $\Delta\phi \sim 0$ V, implying that the orientational change of $TFSA^-$ in the first ionic layer is accompanied by the change in the distance of the polar part of $TFSA^-$. The orientation of ions in the first ionic layer will be discussed in the later section in detail.

The peak shifts of the second ionic layer ($z \sim 8$ Å) were also observed. Specifically, the peak of the second ionic layer for N_{Qa} at positive potentials and N_{BT} at negative potentials shifted toward the IL bulk phase with increasing $|\Delta\phi|$, indicating the increase in the effective thickness of the first ionic layer. The shifts can also be clearly observed in Fig. 3 (a)-(d), by comparing (a) with (b) and (d) with (e). The peak shift at positive potentials was related to the behavior of C_{B4}. In Fig. 3 (b), the first layer peak can be observed for C_{B4} but not for N_{Qa}. Therefore the C_{B4} in the first layer should belong to N^+_{1444} whose N_{Qa} is located at the second layer. This "interlayer crossing" of butyl chain was observed not only from the second to the first layer (Fig. 4 (c)) but also vice versa (Fig. 4 (a)). The N^+_{1444} without the interlayer crossing are also shown in Fig. 4 (b) and (d). Although all the snapshots were taken from the uncharged interface, these were the typical orientations of N^+_{1444} for all the potentials.

MD studies[44,69] for the EDL of ILs using Lennard-Jones sphere model also demonstrated the shift of the ionic layer in the same direction as described above. Compared to these previous studies, a notable characteristic in the present study is the difference in peak shifts between the cation and anion: almost stable peak

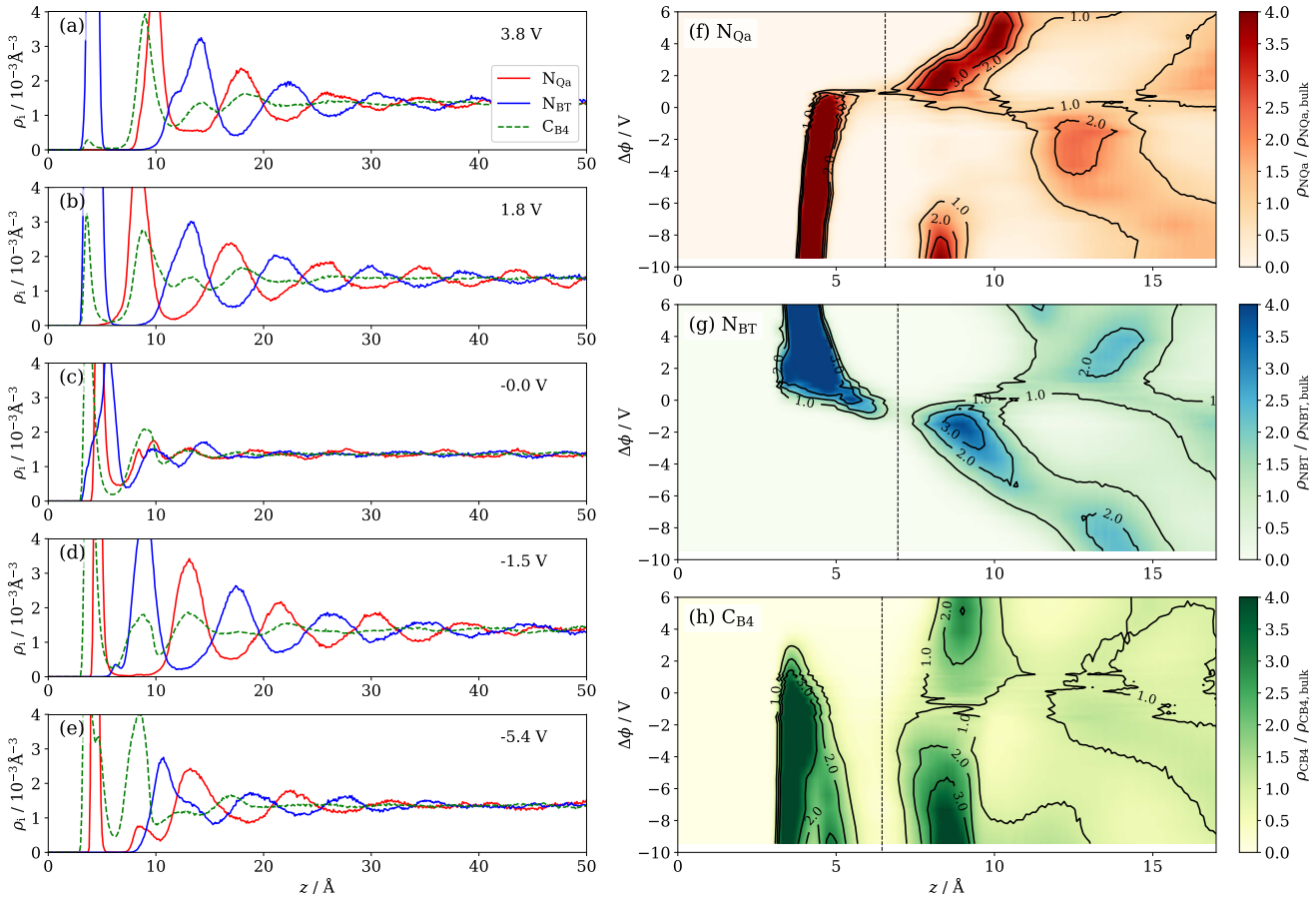

Fig. 3 Number density distributions ρ_i (red; N_{Qa}, blue; N_{BT}, green; C_{B4}) at different potentials ((a)-(e)) and the potential dependence of normalized ρ_i illustrated in contour maps in z-$\Delta\phi$ plane ((f)-(h)). The black vertical dotted lines are the boundary between the first layer and the second layer (z_{div}) for each atom.

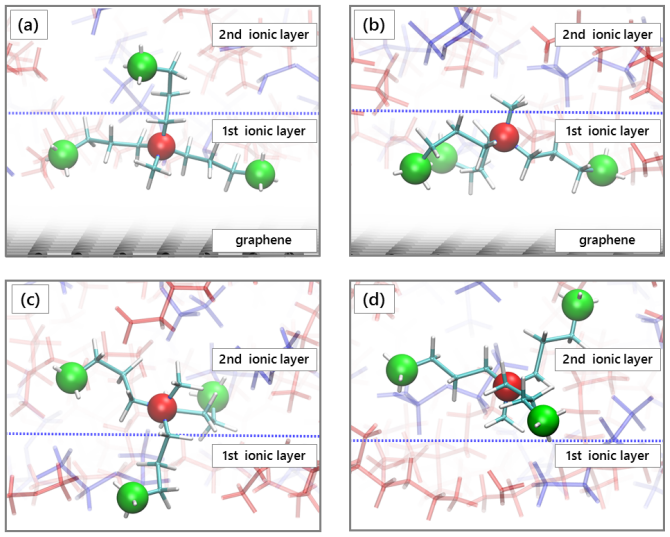

Fig. 4 Side-view snapshots of N^+_{1444}. The electrode is located at the bottom of each figure. (a): N^+_{1444} at the first layer with one butyl group crossing to the second layer (one butyl group perpendicular to and two butyl groups parallel to the electrode). (b): N^+_{1444} at the first layer without crossing to the second layer(all the three butyl groups parallel to the electrode). (c): N^+_{1444} at the second layer with one butyl group crossing to the first layer. (d): N^+_{1444} at the second layer without crossing to the first layer.

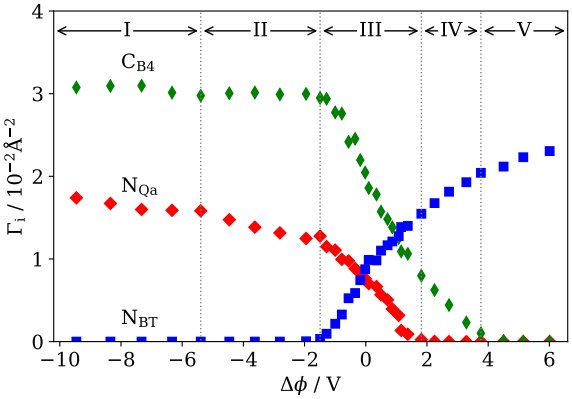

Fig. 5 Surface density of the portion of ions at the first layer (Γ_i; i = N_{Qa} (red), N_{BT} (blue), C_{B4} (green)). The range of the first layer (z = 0 to z_{div}) are shown in Fig. 3(f)-(h). The vertical dotted lines are the potential boundary where the behavior of the Γ_i has changed. I: N^+_{1444} is almost saturated. II: there is still no $TFSA^-$. III: N^+_{1444} and $TFSA^-$ are mixed. IV: the polar part of N^+_{1444} is absent, but the butyl group is still in the first layer. V: the whole part of N^+_{1444} is absent.

position for N_{Qa} and shift for N_{BT} for the first layer, which are the effects of the geometry of polyatomic ions. The former reflects that the closest distance between N_{Qa} and electrode in Fig. 4 (a) and (b) are almost the same. The latter reflects that the closest distance between N_{BT} and electrode depends on the orientation of $TFSA^+$, which will be shown later. Regarding second layer, the dramatic shift for N_{Qa} around 4 V reflects the depletion of the butyl group crossing to the first layer. On the other hand, the gradual shift for N_{BT} at $\Delta\phi \sim 0$ to ~ -6 V reflects the gradual crowding of the butyl group at the first and second layers.

3.2 Composition of first ionic layer

We analyzed the surface density Γ of N_{Qa}, C_{B4}, N_{BT} at the first ionic layer to investigate the change in the composition of the first ionic layer (Fig. 5). As described in the Data analysis section, the Γ values were calculated by integrating the first layer peaks in the number density distribution profiles. Here, note that the ratio of Γ_{CB4} on Γ_{NQa} is not always coincident with three, which is the stoichiometric ratio in a N^+_{1444} cation. This discrepancy is due to independent belongings of N_{Qa} and C_{B4} to layers in the present study. The snapshots are shown in Fig. 4 (a), (b), (c), and (d). In Fig. 4 (a), for example, a C_{B4} atom of an N^+_{1444} is located at the second layer region (z $\sim$ 8 Å) and the N_{Qa} atom of the same N^+_{1444} belongs to the first ionic layer, and therefore the C_{B4} atom is counted as the portion of the second layer.

We focus on the behavior of Γ_i at negative potentials $\Delta\phi = 0$ to -10 V. The potentials can be separated into three regions, which are shown in Fig. 5 as region III, II, and I. First, in the potential region III, as the potential becomes more negative, the increases in Γ_{NQa} and Γ_{CB4}, and the decrease in Γ_{NBT} occurred simultaneously. Second, the III/II boundary is defined as the potential at which N_{BT} disappears from the first ionic layer. In region II, the increasing rate of Γ_{NQa} becomes slower than that in region III. Moreover, Γ_{CB4} is constant in the region II. Third, the II/I boundary is defined as the potential at which Γ_{NQa} becomes constant, and N^+_{1444} starts to form the second ionic layer. In region I, the increase in the number of N^+_{1444} occurs in the second ionic layer rather than the first ionic layer, although one can still see a slight increase in Γ_{NQa}. This phenomenon is the so-called ion crowding, as described before. It is interesting that the behaviors of Γ_{NQa} and Γ_{CB4} are different, which implies the change in the orientation of N^+_{1444}.

We focus on the positive charging process in Fig. 5 from $\Delta\phi = 0$ to 6 V. The III/IV and IV/V boundaries were determined at the potentials at which Γ_{NQa} and Γ_{CB4} become almost zero, respectively. In the whole regions from $\Delta\phi = 0$ to +6 V, Γ_{NBT} increased, but the rate decreased as the potential becomes positive. In region V, there is no butyl chain in the first ionic layer. In spite of the absence of the butyl chain, which decreased along with the increase in Γ_{NBT} in region IV, Γ_{NBT} still increased as the potential becomes more positive in region V. It is likely that cavities between $TFSA^-$ are being filled and well-packed $TFSA^-$ layer is being formed in region V.

3.3 Orientational distribution of butyl chain in N^+_{1444}

The orientational distributions of butyl chain in N^+_{1444}, $p_{NQa\text{-}CB4}(\theta)$, and snapshots of N^+_{1444} at the first ionic layer are shown in Fig. 6. The dependence of $p_{NQa\text{-}CB4}(\theta)$ on the potential is also shown in Fig. S5 as a contour map.

The $p_{NQa\text{-}CB4}(\theta)$ profiles mainly had two peaks for all the potentials: One was a sharp peak at $\theta \sim 100°$, and the other was a broad peak from 0° to 70°. The two peaks indicate that the three butyl chains in N^+_{1444} have two orientational preference. The sharp peak corresponds to the orientation in which a butyl

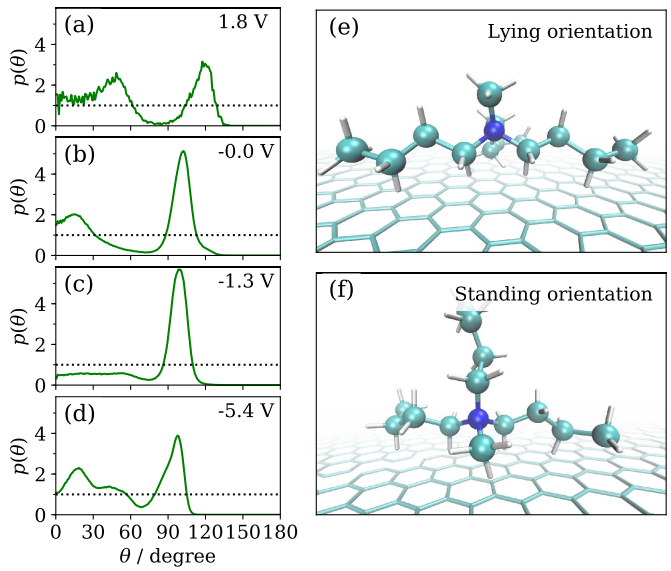

Fig. 6 (a)-(d): Orientational distribution function $p_{NQa-CB4}(\theta)$ of the intramolecular vector N_{Qa}-C_{B4} of N^+_{1444}. (e), (f): Lying and standing orientations of N^+_{1444} in the first layer. The broad peak from 0° to 70° in (a)-(d) corresponds to the butyl group perpendicular to the electrode only appearing in the snapshot (f), whereas the sharp peak at 110° corresponds to those parallel to the electrode appearing in both (e) and (f).

chains is relatively parallel to the electrode. In Fig. 6 (e), all the three butyl chains in N^+_{1444} have this orientation. In the present study, we refer to such orientation of N^+_{1444} in Fig. 6 (e) as "lying orientation." On the other hand, the broad peak in Fig. 6 corresponds to the orientation in which the butyl chain is relatively perpendicular to the electrode. As Fig. 6 (a)-(d) show, the broad peak shifted and splitted depending on the potential, indicating that the peak includes some orientations of the butyl chain. In the present study, we regarded them as the same group of orientation. The snapshot in Fig. 6 (f) is a typical orientation of N^+_{1444} in which one of the butyl chains is relatively perpendicular to the electrode. In the present study, we refer to the orientation of N^+_{1444} as "standing orientation." The snapshot shows that one of the butyl chains stands, but the other two lie in the standing orientation. Therefore, it should be noted that these two orientations of N^+_{1444} do not correspond one-by-one to the two peaks in $p_{NQa-CB4}(\theta)$. It should also be noted that the orientations of butyl chains in a N^+_{1444} are not independent, because they are covalently bonded to the quaternary N atom. This effect was observed as the peak split in Fig. 6 (d). One of the peaks ($\theta \sim 50°$) corresponds to the standing orientation of N^+_{1444} in which two butyl chains stand. Because of mutual exclusion between chains, the orientational angles of standing two butyl chains tend to be larger than that of the one butyl chain standing case as in Fig. 6 (f).

Interestingly, at −1.3 V (Fig. 6 (c)), the "lying" peak of $p_{NQa-CB4}(\theta)$ is the sharpest whereas the "standing" peak is obscure, indicating that the lying orientation of N^+_{1444} is the most predominant at this potential. The standing orientation becomes competitive at the positive potential side or further negative potential (Fig. 7).

3.4 Fraction of orientations of butyl chains

Since Fig. 6 revealed two preferred orientations of butyl chains in N^+_{1444}, we investigate the fraction of these orientations as a function of the potential. To calculate the fraction, we integrated $p_{NQa-CB4}(\theta)$ for θ ranges corresponding to the orientations using eq. (3) and divided by two.

The ranges of θ were from 0° to θ_{div}, and θ_{div} to 180°, where θ_{div} was the orientational angle where $p_{NQa-CB4}(\theta)$ showed the local minimum around $\theta \sim 60°$. The fraction of orientations of butyl chains is shown in Fig. 7 as a function of the potential. The purple plots for the "standing" peak indirectly reflect the amount of standing orientation of N^+_{1444}. Note that the green plots for the "lying" peak reflect both of the standing and lying orientations of N^+_{1444} (Fig. 6 (e) and (f)), but can be an index of the fraction of the lying orientation. The sum of these plots is one for all the potential, which can be easily checked from eq. (3).

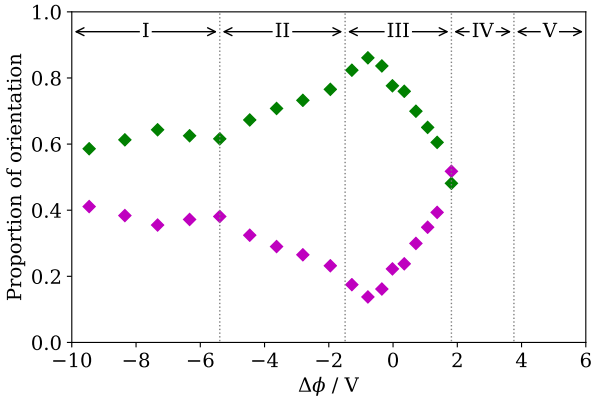

Fig. 7 Fraction of butyl group standing (purple) and lying (green) in the first interface layer. The fraction was calculated by integrating the two peaks in $p_{NQa-CB4}(\theta)$ shown in Fig. 6 based on eq. (3). The marked regions I-V correspond to Fig. 5.

Fig. 7 showed that the fraction of the lying orientation is highest at a negative potential in the potential region III, decreases as the potential becomes more negative in the region II, and is almost constant at the region I.The potential dependence of the fraction of orientations agrees with that of the composition of the first ionic layer (Fig. 5), which was described above.

First, in region III, the fraction of lying orientation increases as the potential becomes more negative, which is likely to contribute to the higher increase rate of Γ_{CB4} than that of Γ_{NQa} in the same region(Fig. 5). Note that the interpretation is not simple because the depletion of N^+_{1444} at the second layer also contributes to the decrease in Γ_{CB4} (See Fig. 4 (c)). Second, in the region II, the lying orientation decreased, although Γ_{CB4} was almost constant(see Fig. 5). Probably the contribution of orientation was compensated by the increase in the number of N^+_{1444} at the first layer, which was observed as the increase in Γ_{NQa}. In other words, the change in the orientation permits the increase in the number of N^+_{1444} in the first layer at the potentials where $TFSA^-$ is absent. The almost constant fraction of the orientation in region I also agrees with the saturation of Γ_{NQa} and development of cationic second layer. In region I, N^+_{1444} is likely to be in the optimal ori-

entation to be fully packed in the first ionic layer.

This orientational behavior may indicate that N^+_{1444} tends to lie the butyl chains with satisfying the number of the cation required by the electroneutrality. This trend can be explained by Asakura-Oosawa theory,[72] for the depletion force between large particles in liquids. When a liquid mixture is composed of large and small molecules, the theory predicts that large molecules prefer to be in contact with solid substrate because of the overlap of excluded volumes of the large molecule and the substrate.[73,74] Although the contact causes a loss of translational entropy of the large molecule, it increases available space for small molecules to move and leads to the gain of their translational entropy, leading to the increase in the total entropy of the system. In the present study, the N^+_{1444} in the lying orientation makes more ions freely translate and therefore, entropically preferable.

The change in orientation of N^+_{1444} affects the electrostatic interaction with neighboring ions as well. The standing butyl chains at positive potentials in region III, where the anions are dominant in the first ionic layer, indicate shorter distance with neighboring anions and stronger in-plane attractive interaction. On the other hand, the lying butyl chains at negative potentials in region III, where oppositely the cations are dominant, implies weaker in-plane repulsive electrostatic interaction with neighboring cations and stronger out-of-plane attractive interaction with anions existing in the second ionic layer. The increase in the proportion of standing butyl chains with decreasing the potential in region II indicates the shorter distance with cations in the in-plane direction and longer distance with anions in the out-of-plane direction, both of which are not energetically preferable but are compensated for by the strong attractive interaction between cations and negative charge on the electrode surface.

3.5 Orientation distribution of $TFSA^-$

To understand the behavior of ions in the first ionic layer the orientations of $TFSA^-$ as well as N^+_{1444} is important. We calculated $p_{\text{i-j}}(\theta)$ of the intra-molecule vectors of $TFSA^-$ in the first ionic layer. The $p_{\text{i-j}}(\theta)$ of S_{BT}-S_{BT} and S_{BT}-C_{BT} are shown in Fig. 8 (a) and (b), respectively, as contour maps as a function of potential and θ.

Here we focus on the behavior in the positive potentials. The peak of $p_{\text{SBT-SBT}}(\theta)$ at $\theta \sim 90°$ increased with increasing the potential, indicating the increase in the orientation of S_{BT}-S_{BT} vector parallel to the electrode. At the same time, the peak of $p_{\text{SBT-CBT}}(\theta)$ at $\theta \sim 90°$ decreased, and that at $\theta \sim 30°$ increased, indicating that the increase in the number of CF_3 groups pointing to the IL bulk. These peaks of $p_{\text{SBT-SBT}}(\theta)$ and $p_{\text{SBT-CBT}}(\theta)$ correspond to the orientation of $TFSA^-$ shown in Fig. 8 (c) and (d). At the positive potentials in regions IV and V, the orientation in Fig. 8 (c) is superior to that in Fig. 8 (d). The orientation of $TFSA^-$ in Fig. 8 (c) occupies a large area on the electrode than the orientation in which the S_{BT}-S_{BT} vector stands. One may expect that $TFSA^-$ stands at the positive potentials, like Fig. 8 (e), similarly to the orientational behavior of N^+_{1444}, in which more N^+_{1444} showed standing orientation as potential become negative. However, such standing orientation of $TFSA^-$ was less observed as the

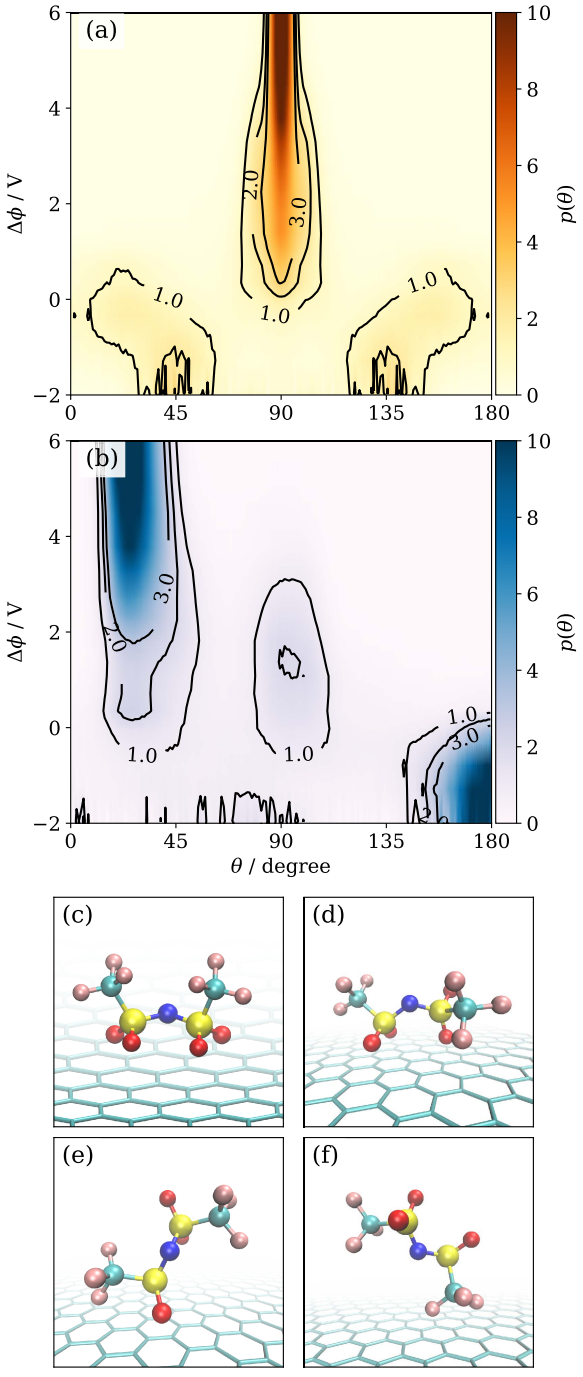

Fig. 8 (a), (b): Contour map of $p_{\text{SBT-SBT}}(\theta)$ (a) and $p_{\text{SBT-CBT}}$ (b) on the $\Delta\phi$-θ plane. (c)-(f): Snapshots of $TFSA^-$ in the first ion layer. In the order of (c)> (d)> (e)> (f), the fraction of the $TFSA^-$'s orientation increases as the potential becomes positive.

potential becomes positive, probably because the standing orientation increases the distance between the electrode and polar-part of $TFSA^-$ (N_{BT} and O_{BT}), which is electrostatically unstable. Furthermore, ions in standing orientation have a loss of entropy compared with that in lying orientation as already discussed with Asakura-Oosawa theory. The standing orientation would permit the larger number of $TFSA^-$ in the first ionic layer, but it does not cause energetic and entropic advantage, unlike the N^+_{1444} case. On the other hand, CF_3 group standing at positive potentials is similar to the orientational behavior of N^+_{1444}.

Next, we focus on negative potentials in Fig. 8. The orientational preferences of $TFSA^-$ were different from those in positive potentials. In Fig. 8 (a), the broad peaks in $p_{\text{SBT-SBT}}(\theta)$ at $\theta \sim 0°$ to $60°$ and $\theta \sim 120°$ to $180°$ were observed, indicating that the vector is standing rather than lying on the electrode. At the same time, for $p_{\text{CBT-SBT}}$ (Fig. 8 (b)) the peak at $\theta \sim 180°$ increased as the potential becomes more negative, indicating that the CF_3 group in $TFSA^-$ points to electrode. When S_{BT}-S_{BT} is relatively standing, a CF_3 group touches the electrode, whereas the other CF_3 group in the same $TFSA^-$ should depart from the surface of the electrode. The orientations of $TFSA^-$ at negative potentials are shown in Fig. 8 (e) and (f). The fraction of Fig. 8 (f) orientation increases as the potential becomes more negative. The drastic change in the orientational preference from positive to negative potential also agreed with the peak shift of the first ionic layer shown in number density distribution of N_{BT} in Fig. 3 (g).

3.6 Schematic EDL structure

The EDL structure of $[N^+_{1444}][TFSA^-]$ revealed by number density and orientational distributions are summarized as a schematic image in Fig. 9. In the negative side of region III, the lying orientation of N^+_{1444} increases as the potential becomes more negative. Simultaneously, a CF_3 group in $TFSA^-$ departs from the surface of the electrode. At the II/III boundary, $TFSA^-$ completely disappears from the first ionic layer. However, at the more negative potentials in region II, N^+_{1444} still increases in the number because of the change in the orientation of N^+_{1444} from lying to standing. At the I/II boundary N^+_{1444} in the first ionic layer becomes saturated. At the more negative potentials in region I, the increase in N^+_{1444} occurs in the second ionic layer.

In the positive side of region III, $TFSA^-$ prefers the orientation in which the S_{BT}-S_{BT} vector is parallel to the electrode. The polar-part (N_{Qa}) of N^+_{1444} departs from the electrode as the potential becomes more positive. At the III/IV boundary, N^+_{1444} disappears from the first ionic layer, but a butyl chain in the N^+_{1444} remains in the first layer region. Hence, in the potentials in region IV, the accumulation of $TFSA^-$ in the first ionic layer occurs removing the butyl chain from the layer, i.e., changing in the orientation of N^+_{1444} at the second ionic layer. At more positive potentials in region V, the butyl chain completely departs from the first ionic layer, but the accumulation of $TFSA^-$ still occur with increasing potential. $TFSA^-$ presumably form a better packing structure by filling cavities between $TFSA^-$ ions and optimizing the structure of $TFSA^-$. $TFSA^-$ in the first ionic layer was not saturated within the potential region investigated in the present study.

3.7 Two Dimensional EDL structure

Since the structural changes shown above involves the change in in-plane structure of the first layer, here we analyzed two dimensional radial distribution function $g_{xy,\text{i}}$ of N_{Qa} and N_{BT} in the first layer. Fig. 10 (a) and (b) show the potential dependence of $g_{xy,\text{i}}$. Fig. 10 (c), (d), (e), (f), and (g) show snapshots of the first layer at different potentials. In the snapshot, the ions and electrode are shown as a stick except for N_{Qa} (red sphere), CB4 (green sphere), and N_{BT} (blue sphere).

First, we focus on N^+_{1444} (Fig. 10 (a)) and look at the change from positive to negative potentials. In region III, the first peak of the $g_{xy,\text{NQa}}$ appeared at $r_{xy} \sim 11$ Å at the most positive potential and shifted to the smaller r_{xy} as the potential become more negative. The peak shift means that the more $TFSA^-$ depleted from the first layer, and the more N^+_{1444} become adjacent to each other. On the other hand, in region II, the peak at $r_{xy} = 9$ Å did not show an apparent shift but became broader at the negative potentials. The broader peak indicates that N^+_{1444} in lying orientation become dominant at negative potentials, and therefore butyl groups are interposed between N_{Qa} (Fig. 10 (d)). Such butyl groups enhance the degree of freedom for the nearest neighbor distance of N_{Qa}. In addition, in region I, a new peak appeared $r_{xy} \sim 6$ Å. The new peak indicates that N_{Qa} of N^+_{1444} in standing orientation are adjacent to each other without the interposed butyl groups(Fig. 10 (c)).

Regarding $TFSA^-$, focusing on the change from negative to positive potentials, the similar tendencies were observed; the peak shift (region III) and the appearance of a new peak (Region IV). However, this new peak was not as clear as N^+_{1444} probably because the first layer was not yet saturated with $TFSA^-$ in Region IV (Fig. 10 (g)). The appearance of the clearer peak can be inferred at the more positive potentials.

The highly-ordered two-dimensional structure of ionic liquids near electrode has been proposed by MD,[45] AFM[75,76] and STM.[39] In the present study, although $g_{xy,\text{i}}$ showed neighboring distances, the high-ordered structure, such as hexagonal and linear, was not observed. Probably, the complex structure of N^+_{1444} in the first layer due to the three butyl chains does not allow such highly-ordered and well-packed structure.

3.8 Differential capacitance

Differential capacitance, C_d, of $[N^+_{1444}][TFSA^-]$ as a function of potential is shown in Fig. 11. The plots in region I and III are highlighted in blue and red for the later discussion. The error bars are the standard errors given by quadratic regression of potential-surface charge density plot (Fig. S3).

The C_d-$\Delta\phi$ plot (Fig. 11) was camel-shaped with two local maxima at ~ -0.2 and $\sim +1.1$ V. According to the mean-field lattice gas model[5] proposed by Kornyshev, in the U-shaped region between the two maxima where the electrode is moderately charged, the excluded volume effect between ions is less prominent, leading to the Gouy-Chapman model[6,7] like behavior. In contrast, the C_d decrease outside the U-shaped region reflects the excluded-volume effect between ions.

The camel shape was significantly asymmetric with respect to

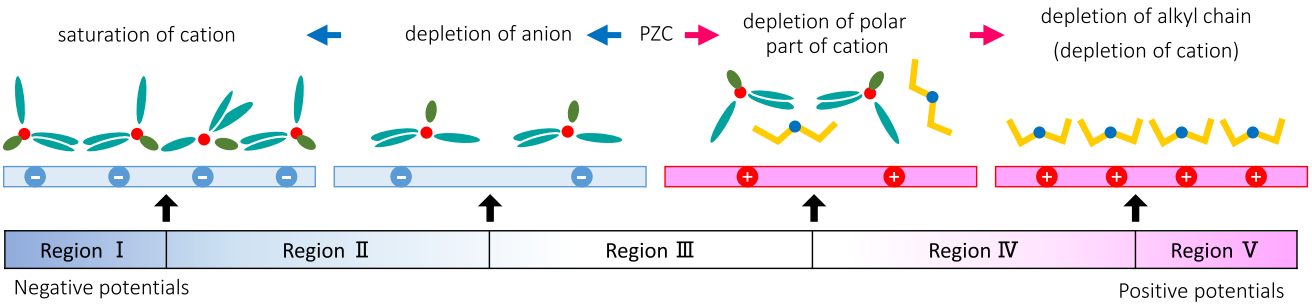

Fig. 9 Schematic illustration of the behavior of $[N^{+}_{1444}][TFSA^{-}]$ at the electric double layer.

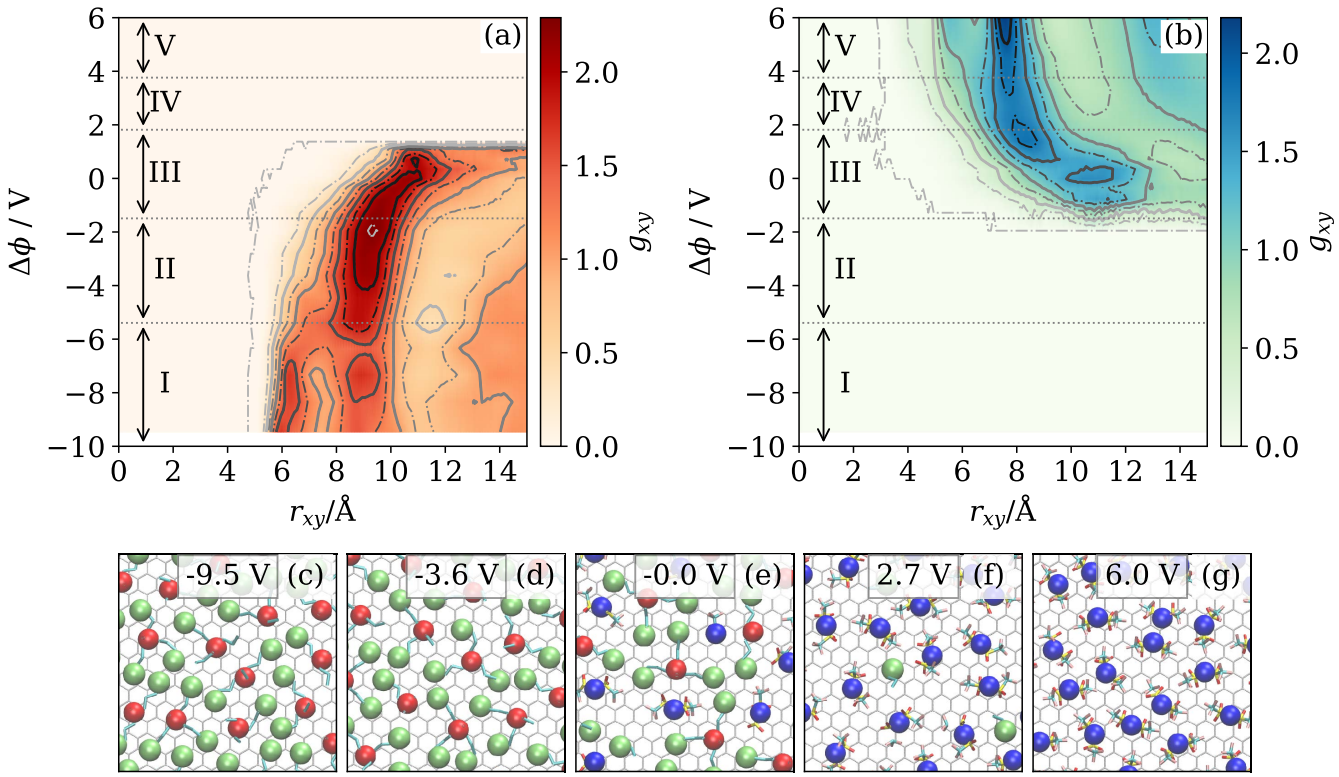

Fig. 10 (a), (b): Contour maps of two dimensional radial distribution function $g_{xy,i}(r_{xy,i})$ for N_{Qa} (a) and N_{BT} (b). The marked regions Ⅰ-Ⅴ correspond to Fig. 5. (c)-(d): Snapshots of first layer viewed from the top at different potentials. N_{Qa} (red), N_{BT} (blue), and C_{B4} (green) are highlighted as spheres.

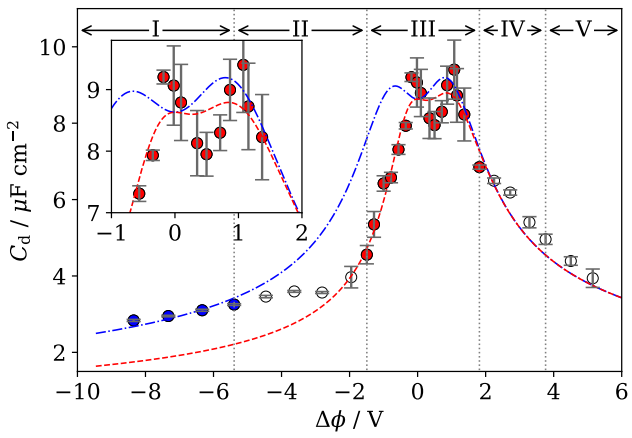

Fig. 11 C_d-$\Delta\phi$ plot. The red dashed line is the fitting curve of a theoretical equation of lattice gas model[10] by Goodwin *et al.* (eq. (7)) to the red plots. The blue dashed-dotted line is the fitting curve to the blue plots when the parameters are fixed to that of the red dashed line except for the parameter of the cation (γ_+). The marked regions I-V correspond to Fig. 5.

the local minimum at $\Delta\phi \sim 0.5$ V (see the inset in Fig. 11). Specifically, the slope at the negative potentials (−2 to 0 V) was steeper than that in the positive potentials (+1 to +4 V). Moreover, the slope at the more negative potentials (< −2 V) became constant. By the mean-field lattice gas model,[5] such kind of asymmetric $\Delta\phi$-C_d curve has been explained as a result of the difference in the size of cation and anion. Qualitatively, the model suggests that when C_d is higher at positive than at negative potentials the anion is smaller than the cation, which agrees with the DFT calculation results of the volume of N^+_{1444} and $TFSA^-$ described above.

To quantitatively analyze the C_d-$\Delta\phi$ plot, we utilized the C_d formula derived by the lattice gas model which was recently proposed by Goodwin et al.[10] In the formula, C_d is expressed as a function of potential as follows,

$$C_d = \tilde{C}_{d0}\frac{\cosh(\alpha u_0/2)}{1+2\gamma\sinh^2(\alpha u_0/2)}\sqrt{\frac{2\gamma\sinh^2(\alpha u_0/2)}{\ln(1+2\gamma\sinh^2(\alpha u_0/2))}} \quad (7)$$

where $u_0 = \frac{e\Delta\phi}{k_B T}$ is reduced potential at the electrode, $\tilde{C}_{d0}$ is C_d at PZC, α is a factor representing the short-range repulsive / attractive interactions between co-ions / counter ions, and γ is compacity, which represents the condensation capability of the ion at the EDL. γ is expressed as $\gamma = 2C_{bulk}/C_{max}$, where C_{bulk} is the concentration of ions in bulk and C_{max} is the maximum concentration of ions at EDL. For the case of the present study, different γ values of N^+_{1444} and $TFSA^-$ (γ_+ and γ_-) should be defined because they have different C_{max}. The γ values are approximately expressed[5] as a function of u_0 as follows,

$$\gamma = \gamma_- + \frac{\gamma_+ - \gamma_-}{1+\exp(\alpha u_0).} \quad (8)$$

We fitted the formula to the C_d-$\Delta\phi$ plot of $[N^+_{1444}][TFSA^-]$ obtained in the present study. The fitting parameters are $\tilde{C}_{d0}, \alpha, \gamma_+$, and γ_-. The best fit parameters are listed in Table 1.

The curve fitted for all plots is shown in Fig. S6. As Fig. S6 shows, the lattice gas model reproduced the C_d for the regions III, IV, and V, although it could not reproduce that for the regions I and II. It is inadequate to discuss the theoretical curve given by the fitting including the plots beyond the model. Hence, we limited the fitting region to the region III. This fitted curve is shown as a red dashed line in Fig. 11. The newly fitted curve was similar to the old curve (see Fig. S6 to compare them).

For C_d-$\Delta\phi$ plot compared with the fitted curve, there are the small discrepancies at positive potentials and large discrepancy at negative potentials. The former implies that the replacement of $TFSA^-$ with N^+_{1444} can basically be interpreted within the lattice gas model. The latter large discrepancy indicates that there is also a discrepancy in the behaviors of ions between the lattice gas model and N^+_{1444} in region I and II where $TFSA^-$ is depleted at the first layer. The most likely reason is the change in orientational preference of N^+_{1444} from lying to standing as the potential becomes more negative in region II (Fig. 7), because the lattice gas model does not consider orientational effect explicitly. A N^+_{1444} in the standing orientation occupies a significantly smaller area on the electrode than that in the lying orientation. Therefore the increase in the fraction of standing orientation causes the increase in the C_{max} of N^+_{1444}. In the representation of the lattice gas model, $[N^+_{1444}][TFSA^-]$ should have smaller γ_+ at highly negative potentials compared with the apparent γ_+ around PZC.

To test the idea, we fixed the parameters ($\tilde{C}_{d0}$, α, γ_-) other than γ_+, and fitted the formula to the plots in region I. As a result, the fitted curve (blue dashed-dotted line) reproduced the plots in region I, indicating that the orientational effect on C_{max} has an important role to the $\Delta\phi$-C_d curve. Describing explicit orientational effect is a possible extension of the lattice gas model. In a simple way, this may be done by modifying eq. 8 to describe decrease in γ at negative potentials.

Comparison of the present simulation results with experimental ones would be worthful. First of all, in our previous zero-frequency C_d measurement using the electrocapillarity,[21] the value of γ_- in 1-ethyl-3-methylimidazolium (C^+_{2mim}) $TFSA^-$ was found to be 0.5 by fitting using a lattice gas model,[8] whereas the γ_- value for $TFSA^-$ (~ 0.2) in the present study is significantly smaller. According to the lattice gas model,[5] γ ($= 2C_{bulk}/C_{max}$) of an ion is not specific to the ion but depends on the counter ion because the latter affects C_{bulk}. The larger size of N^+_{1444} than C^+_{2mim} leads to the smaller C_{bulk} and then smaller γ_- in $[N^+_{1444}][TFSA^-]$ than $[C^+_{2mim}][TFSA^-]$. On the other hand, the entire C_d values are significantly smaller than the experimental values, even taking into account differences between QaILs and imidazolium-based ILs. The difference between potentials at the two maxima of the camel shape are larger than that in 1-octyl-3-methylimidazolium BF_4^-.[20] To obtain further information on the discrepancies the comparison would be helpful with experimental zero-frequency C_d of $[N^+_{1444}][TFSA^-]$ by using the pendant drop method[20,21]. The measurement and the analysis are in progress in our laboratory.

4 Conclusions

Focusing on N^+_{1444}, which is a quaternary-ammonium cation having three long-chain alkyl groups, we clarified the potential de-

Table 1 Best fit parameters of the fitting using theoretical equation of lattice gas model[10] by Goodwin *et al.*

range of $\Delta\phi$ for fitting / V	C_0 / μFcm^{-2}	γ_+	γ_-	α
−8.3 to 5.1 (whole range)	8.6 ± 0.3	0.56 ± 0.09	0.24 ± 0.03	0.09 ± 0.01
−1.5 to 1.8	8.6 ± 0.2	0.6 ± 0.1	0.23 ± 0.02	0.09 ± 0.01
−8.3 to −5.4	8.6 (fixed)	0.26 ± 0.01	0.23 (fixed)	0.09 (fixed)

pendence of the electric double layer structure and differential capacitance at the interface between $[N^+_{1444}][TFSA^-]$ and graphene electrode. The composition of the first layer was evaluated based on the surface density of the polar parts of N^+_{1444} and $TFSA^-$, and the butyl group in N^+_{1444}. From the first layer composition, the potential was found to be divided into five regions. In particular, at negative potentials, the number of polar parts of N^+_{1444} increased as the potential became negative even at the potentials where the butyl group saturated in the first layer (region II).

Orientational analysis of the butyl group in the first layer revealed that N^+_{1444} has the orientational change from lying to standing as the potential becomes negative in the region II. Standing orientation is not entropically favored because it reduces the entropic gain originating from the translational movement of ions in the IL bulk. Therefore, the standing orientation became competitive only in the positive and negative potential regions where the electrostatic energy between ions and electrode is large.

The C_d-$\Delta\phi$ plot was camel-shaped, and its behavior around $\Delta\phi$ = 0 V was reproduced by fitting the theoretical formula of the lattice gas model. However, C_d had a discrepancy between the fitting curve and the MD values at potentials in region II and at the more negative potentials. The discrepancy is correlated with the change in orientation of N^+_{1444}. The decrease in C_d at negative potentials is likely to be alleviated by the change in orientation of N^+_{1444}.

Conflicts of interest

There are no conflicts to declare.

Acknowledgements

This work was partly supported by JSPS KAKENHI (No. 18K05171), TEPCO Memorial Foundation, and Kato Foundation for Promotion of Science.

References

1 A. Lewandowski and A. Swiderska-Mocek, *J. Power Sources*, 2009, **194**, 601–609.
2 M. P. S. Mousavi, B. E. Wilson, S. Kashefolgheta, E. L. Anderson, S. He, P. Bühlmann and A. Stein, *ACS Appl. Mater. Interfaces*, 2016, **8**, 3396–3406.
3 S. Y. Lee, A. Ogawa, M. Kanno, H. Nakamoto, T. Yasuda and M. Watanabe, *J. Am. Chem. Soc.*, 2010, **132**, 9764–9773.
4 M. Armand, F. Endres, D. R. MacFarlane, H. Ohno and B. Scrosati, *Nat. Mater*, 2009, **8**, 621–629.
5 A. A. Kornyshev, *J. Phys. Chem. B*, 2007, **111**, 5545–5557.
6 D. L. Chapman, *Phil. Mag.*, 1913, **25**, 475–481.
7 M. Gouy, *J. Phys. Theor. Appl.*, 1910, **9**, 457–468.
8 Y. Han, S. Huang and T. Yan, *J. Phys. Condens. Matter*, 2014, **26**, 284103.
9 A. C. Maggs and R. Podgornik, *Soft Matter*, 2016, **12**, 1219–1229.
10 Z. A. H. Goodwin, G. Feng and A. A. Kornyshev, *Electrochim. Acta*, 2017, **225**, 190–197.
11 R. Downing, B. K. Berntson, G. V. Bossa and S. May, *J. Chem. Phys.*, 2018, **149**, 204703.
12 J. Vatamanu, O. Borodin and G. D. Smith, *J. Am. Chem. Soc.*, 2010, **132**, 14825–14833.
13 J. Vatamanu, O. Borodin, D. Bedrov and G. D. Smith, *J. Phys. Chem. C*, 2012, **116**, 7940–7951.
14 Z. Z. Hu, J. Vatamanu, O. Borodin and D. Bedrov, *Electrochim. Acta*, 2014, **145**, 40–52.
15 J. B. Haskins and J. W. Lawson, *J. Chem. Phys.*, 2016, **144**, 184707.
16 M. M. Islam, M. T. Alam and T. Ohsaka, *J. Phys. Chem. C*, 2008, **112**, 16568–16574.
17 V. Lockett, R. Sedev, J. Ralston, M. Horne and T. Rodopoulos, *J. Phys. Chem. C*, 2008, **112**, 7486–7495.
18 B. Roling, M. Druschler and B. Huber, *Faraday Discuss.*, 2012, **154**, 303–311.
19 T. Jansch, J. Wallauer and B. Roling, *J. Phys. Chem. C*, 2015, **119**, 4620–4626.
20 N. Nishi, A. Hashimoto, E. Minami and T. Sakka, *Phys. Chem. Chem. Phys.*, 2015, **17**, 5219–5226.
21 N. Nishi, S. Yasui, A. Hashimoto and T. Sakka, *J. Electroanal. Chem.*, 2017, **789**, 108–113.
22 N. Nishi, Y. Kojima, S. Katakura and T. Sakka, *Electrochemistry*, 2018, **86**, 38–41.
23 K. Motobayashi, K. Minami, N. Nishi, T. Sakka and M. Osawa, *J. Phys. Chem. Lett.*, 2013, **4**, 3110–3114.
24 K. Motobayashi, N. Nishi, Y. Inoue, K. Minami, T. Sakka and M. Osawa, *J. Electroanal. Chem.*, 2017, **800**, 126–133.
25 A. Uysal, H. Zhou, G. Feng, S. S. Lee, S. Li, P. Fenter, P. T. Cummings, P. F. Fulvio, S. Dai, J. K. McDonough and Y. Gogotsi, *J. Phys. Chem. C*, 2014, **118**, 569–574.
26 S. Makino, Y. Kitazumi, N. Nishi and T. Kakiuchi, *Electrochem. Commun.*, 2011, **13**, 1365–1368.
27 N. Nishi, Y. Hirano, T. Motokawa and T. Kakiuchi, *Phys. Chem. Chem. Phys.*, 2013, **15**, 11615–11619.
28 A. Uysal, H. Zhou, G. Feng, S. S. Lee, S. Li, P. T. Cummings, P. F. Fulvio, S. Dai, J. K. McDonough, Y. Gogotsi and P. Fenter, *J. Phys. Condens. Matter*, 2015, **27**, 032101.
29 M. Mezger, H. Schröder, H. Reichert, S. Schramm, J. S. Okasinski, S. Schröder, V. Honkimäki, M. Deutsch, B. M. Ocko, J. Ralston, M. Rohwerder, M. Stratmann and H. Dosch, *Science*, 2008, **322**, 424–428.
30 H. Zhou, M. Rouha, G. Feng, S. S. Lee, H. Docherty, P. Fenter,

P. T. Cummings, P. F. Fulvio, S. Dai, J. McDonough, V. Presser and Y. Gogotsi, *ACS Nano*, 2012, **6**, 9818–9827.
31 N. Nishi, T. Uruga and H. Tanida, *J. Electroanal. Chem.*, 2015, **759**, 129–136.
32 M. Chu, M. Miller and P. Dutta, *ACS Cent. Sci.*, 2016, **2**, 175–180.
33 P. Reichert, K. S. Kjaer, T. Brandt van Driel, J. Mars, J. W. Ochsmann, D. Pontoni, M. Deutsch, M. M. Nielsen and M. Mezger, *Faraday Discuss.*, 2017, **206**, 141–157.
34 Y. Lauw, M. D. Horne, T. Rodopoulos, V. Lockett, B. Akgun, W. A. Hamilton and A. R. Nelson, *Langmuir*, 2012, **28**, 7374–7381.
35 N. Nishi, J. Uchiyashiki, Y. Ikeda, S. Katakura, T. Oda, M. Hino and N. L. Yamada, *J. Phys. Chem. C*, 2019, **123**, 9223–9230.
36 R. Atkin and G. G. Warr, *J. Phys. Chem. C*, 2007, **111**, 5162–5168.
37 F. Endres, N. Borisenko, S. Z. El Abedin, R. Hayes and R. Atkin, *Faraday Discuss.*, 2012, **154**, 221–233.
38 S. Perkin, *Phys. Chem. Chem. Phys.*, 2012, **14**, 5052–5062.
39 Y. Z. Su, Y. C. Fu, J. W. Yan, Z. B. Chen and B. W. Mao, *Angew. Chem. Int. Ed.*, 2009, **48**, 5148–5151.
40 S. Baldelli, *Acc. Chem. Res.*, 2008, **41**, 421–431.
41 S. Y. Xu, S. R. Xing, S. S. Pei, V. Ivaništšev, R. Lynden-Bell and S. Baldelli, *J. Phys. Chem. C*, 2015, **119**, 26009–26019.
42 S. G. Harroun, T. J. Abraham, C. Prudhoe, Y. Zhang, P. J. Scammells, C. L. Brosseau, C. C. Pye and R. D. Singer, *Phys. Chem. Chem. Phys.*, 2013, **15**, 19205–19212.
43 J. C. Rubim, F. A. Trindade, M. A. Gelesky, R. F. Aroca and J. Dupont, *J. Phys. Chem. C*, 2008, **112**, 19670–19675.
44 V. Ivaništšev and M. V. Fedorov, *Electrochem. Soc. Interface*, 2014, **23**, 65–69.
45 S. A. Kislenko, I. S. Samoylov and R. H. Amirov, *Phys. Chem. Chem. Phys.*, 2009, **11**, 5584–5590.
46 R. M. Lynden-Bell, A. I. Frolov and M. V. Fedorov, *Phys. Chem. Chem. Phys.*, 2012, **14**, 2693–2701.
47 S. Sharma and H. K. Kashyap, *J. Phys. Chem. C*, 2015, **119**, 23955–23967.
48 S. Sharma and H. K. Kashyap, *J. Phys. Chem. C*, 2017, **121**, 13202–13210.
49 S. Sharma, H. S. Dhattarwal and H. K. Kashyap, *J. Mol. Liq.*, 2019, **291**, 111269.
50 N. Nishi, K. Minami, K. Motobayashi, M. Osawa and T. Sakka, *J. Phys. Chem. C*, 2017, **121**, 1658–1666.
51 N. Nishi, Y. Ikeda and T. Sakka, *J. Electroanal. Chem.*, 2018, **817**, 210–216.
52 N. Nishi, Y. Yasui, T. Uruga, H. Tanida, T. Yamada, S. Nakayama, H. Matsuoka and T. Kakiuchi, *J. Chem. Phys.*, 2010, **132**, 164705.
53 N. Nishi, T. Uruga, H. Tanida and T. Kakiuchi, *Langmuir*, 2011, **27**, 7531–7536.
54 S. Katakura, N. Nishi, K. Kobayashi, K.-i. Amano and T. Sakka, *J. Phys. Chem. C*, 2019, **123**, 7246–7258.
55 W. Smith and T. R. Forester, *J. Mol. Graph.*, 1996, **14**, 136–141.
56 J. N. Canongia Lopes and A. A. H. Pádua, *J. Phys. Chem. B*, 2004, **108**, 16893–16898.
57 W. L. Jorgensen, D. S. Maxwell and J. TiradoRives, *J. Am. Chem. Soc.*, 1996, **118**, 11225–11236.
58 U. Essmann, L. Perera, M. L. Berkowitz, T. Darden, H. Lee and L. G. Pedersen, *J. Chem. Phys.*, 1995, **103**, 8577–8593.
59 I. Leontyev and A. Stuchebrukhov, *Phys. Chem. Chem. Phys.*, 2011, **13**, 2613–26.
60 C. Schröder, *Phys. Chem. Chem. Phys.*, 2012, **14**, 3089–102.
61 V. Chaban, *Phys. Chem. Chem. Phys.*, 2011, **13**, 16055–16062.
62 H. J. C. Berendsen, J. P. M. Postma, W. F. van Gunsteren, A. DiNola and J. R. Haak, *J. Chem. Phys.*, 1984, **81**, 3684–3690.
63 S. C. Harvey, R. K. Z. Tan and T. E. Cheatham Iii, *J. Comput. Chem.*, 1998, **19**, 726–740.
64 S. Nose, *Mol. Phys.*, 1984, **52**, 255–268.
65 W. G. Hoover, *Phys. Rev. A. Gen. Phys.*, 1985, **31**, 1695–1697.
66 G. Bussi, D. Donadio and M. Parrinello, *J. Chem. Phys.*, 2007, **126**, 014101.
67 K. I. Amano, Y. Yokota, T. Ichii, N. Yoshida, N. Nishi, S. Katakura, A. Imanishi, K. I. Fukui and T. Sakka, *Phys. Chem. Chem. Phys.*, 2017, **19**, 30504–30512.
68 K. Amano, T. Hayashi, K. Hashimoto, N. Nishi and T. Sakka, *Journal of Molecular Liquids*, 2018, **257**, 121–131.
69 V. Ivaništšev, K. Kirchner, T. Kirchner and M. V. Fedorov, *J. Phys. Condens. Matter*, 2015, **27**, 102101.
70 M. Z. Bazant, B. D. Storey and A. A. Kornyshev, *Phys. Rev. Lett.*, 2011, **106**, 046102.
71 M. J. Frisch, G. W. Trucks, H. B. Schlegel, G. E. Scuseria, M. A. Robb, J. R. Cheeseman, G. Scalmani, V. Barone, B. Mennucci, G. A. Petersson, H. Nakatsuji, M. Caricato, X. Li, H. P. Hratchian, A. F. Izmaylov, J. Bloino, G. Zheng, J. L. Sonnenberg, M. Hada, M. Ehara, K. Toyota, R. Fukuda, J. Hasegawa, M. Ishida, T. Nakajima, Y. Honda, O. Kitao, H. Nakai, T. Vreven, J. A. Montgomery, J. E. Peralta, F. Ogliaro, M. Bearpark, J. J. Heyd, E. Brothers, K. N. Kudin, V. N. Staroverov, R. Kobayashi, J. Normand, K. Raghavachari, A. Rendell, J. C. Burant, S. S. Iyengar, J. Tomasi, M. Cossi, N. Rega, J. M. Millam, M. Klene, J. E. Knox, J. B. Cross, V. Bakken, C. Adamo, J. Jaramillo, R. Gomperts, R. E. Stratmann, O. Yazyev, A. J. Austin, R. Cammi, C. Pomelli, J. W. Ochterski, R. L. Martin, K. Morokuma, V. G. Zakrzewski, G. A. Voth, P. Salvador, J. J. Dannenberg, S. Dapprich, A. D. Daniels, Farkas, J. B. Foresman, J. V. Ortiz, J. Cioslowski and D. J. Fox, *Gaussian 09, Revision B.01*, 2009.
72 F. Oosawa and S. Asakura, *J. Chem. Phys.*, 1954, **22**, 1255–1256.
73 M. Kinoshita, *Chemical Engineering Science*, 2006, **61**, 2150–2160.
74 R. Fantoni and A. Santos, *Phys. Rev. E*, 2013, **87**, 042102.
75 A. Elbourne, S. McDonald, K. Voichovsky, F. Endres, G. G. Warr and R. Atkin, *ACS Nano*, 2015, **9**, 7608–7620.
76 W. Y. Tsai, J. Come, W. Zhao, R. X. Wang, G. Feng, B. P. Thapaliya, S. Dai, L. Collins and N. Balke, *Nano Energy*, 2019, **60**,

886–893.

Supplementary Information: Electric double layer structure and differential capacitance at the electrode interface of tributylmethylammonium bis(trifluoromethanesulfonyl)amide studied using molecular dynamics simulation.

Seiji Katakura, Naoya Nishi,* Kazuya Kobayashi, Ken-ichi Amano and Tetsuo Sakka

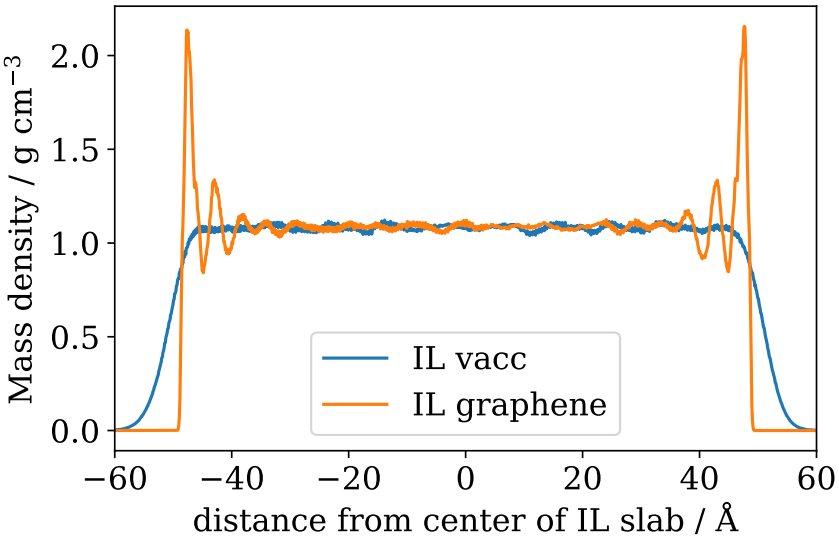

Figure S1: Mass density distribution of $[N^+_{1444}][TFSA^-]$ slab at the vacuum interface and the graphene interface.

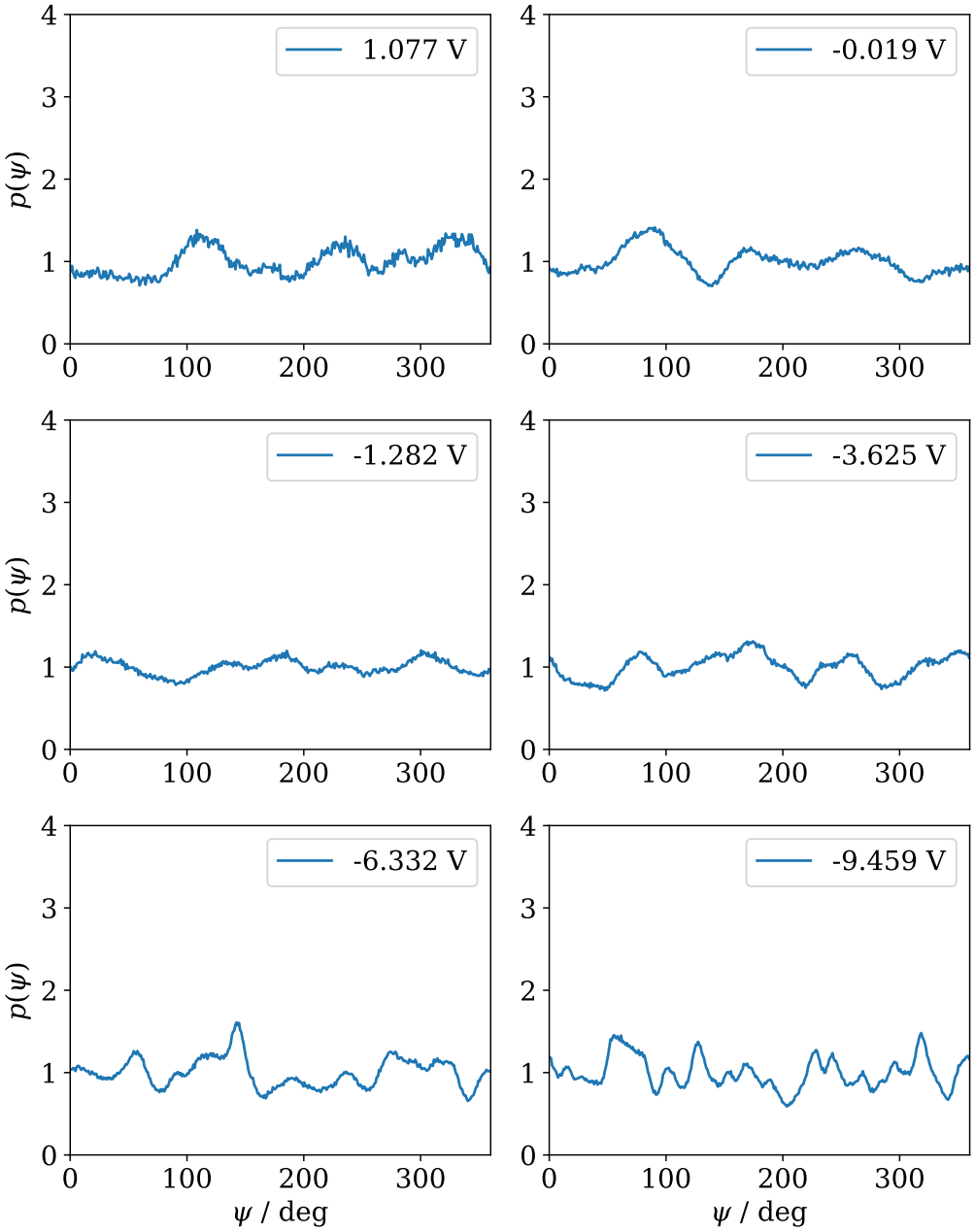

Figure S2: Orientational distribution on azimuthal angle $p(\psi) = \int_0^\pi p(\theta, \psi) \mathrm{d}\theta$.

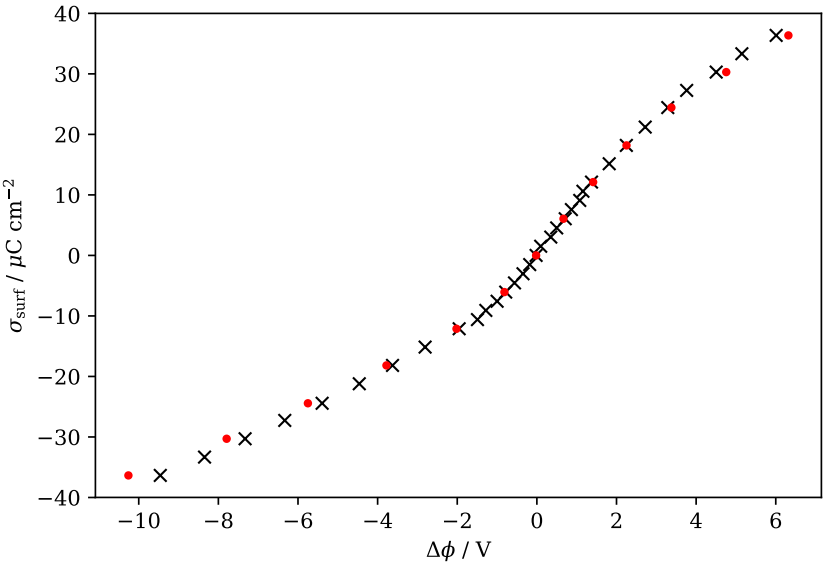

Figure S3: Relationship between the given surface charge density of electrode σ_{elec} and the calculated interfacial potential difference $\Delta\phi$. Black plots; results using SPME. Red plots; results using SPME with slab correction.[1]

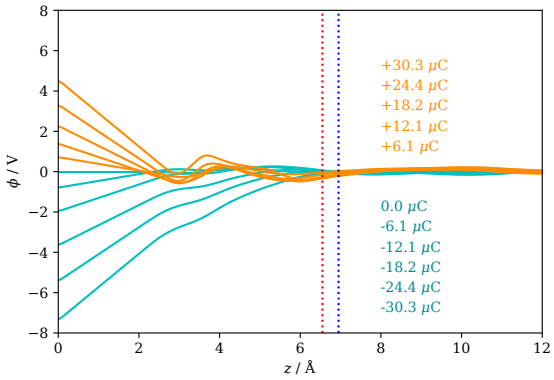

Figure S4: Potential profiles as a function of the distance from electrode (z). The potential at IL_{bulk} was set to be zero. The dotted lines are the border between the first and second layers (z_{div}) of N_{Qa} (red) and N_{BT} (blue).

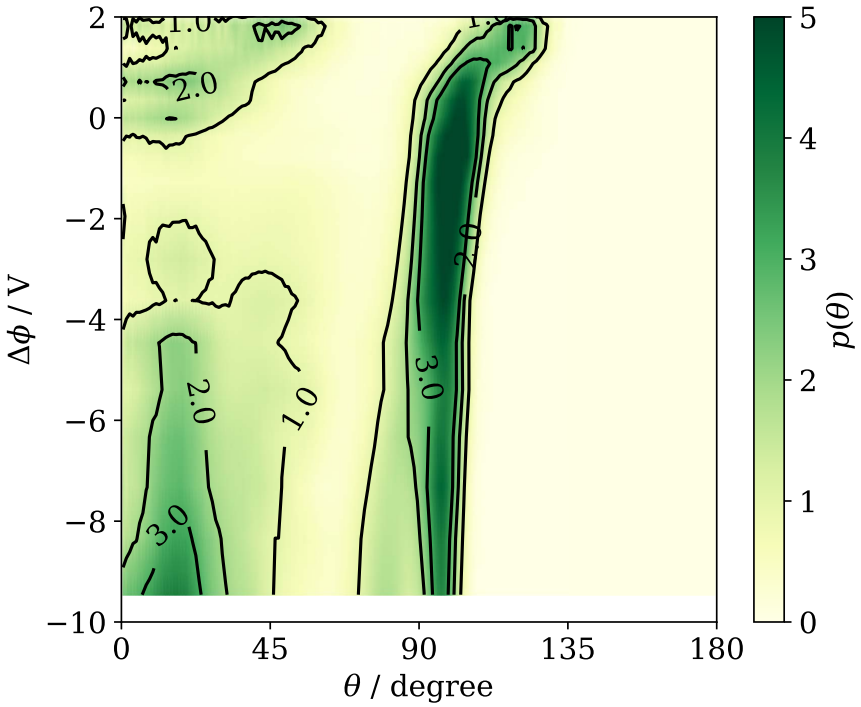

Figure S5: Contour map of $p_{NQa\text{-}CB4}(\theta)$ on the $\Delta\phi$-θ plane.

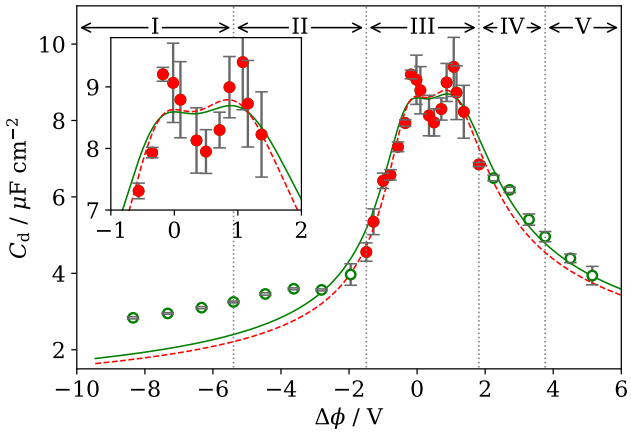

Figure S6: $\Delta\phi$-C_d plot. The plot and red dashed line are the same as in Fig.11. The green solid line is the fitting curve to all the plots. There is no qualitative difference between the red dashed line and the green solid line.

References

[1] I.-C. Yeh and M. L. Berkowitz, *J. Chem. Phys.*, 1999, **111**, 3155–3162.

Manuscript ID: CP-ART-09-2019-005297.R1

****

REVIEWER REPORT(S):

Referee: 1

Comments to the Author

The authors have satisfactorily addressed all the comments I raised, except the first one. In the first comment, we asked about the equilibration criteria followed to ensure the complete equilibration of the IL confined within the sheets for all the systems (charged and uncharged). However, the authors have provided the time evolution of potential developed at the respective electrodes that will only reflect the arrangement of interfacial distribution of IL and will not give the evidence for thoroughly equilibrated IL confined in the

graphene sheets. The authors need to plot the potential energy of whole trajectory for all systems as a function of time, and then analyze the slope of this energy. Along with that, the authors refrain to mention the number of ion pairs used for the investigation. These minor points need to be addressed before the acceptance of the manuscript for publication.

【Author reply】

We appreciate the referee's careful reading. Fig.R1 shows an example of the potential energy per ion in the MD cell as a function of time when the surface charge density on the electrode was changed from 0 to 21.2 μC cm^{-2} at $t = 0$. The potential energy rapidly decays, and the slope from 1 to 3 ns was small enough to analyze the system as an equilibrium state.

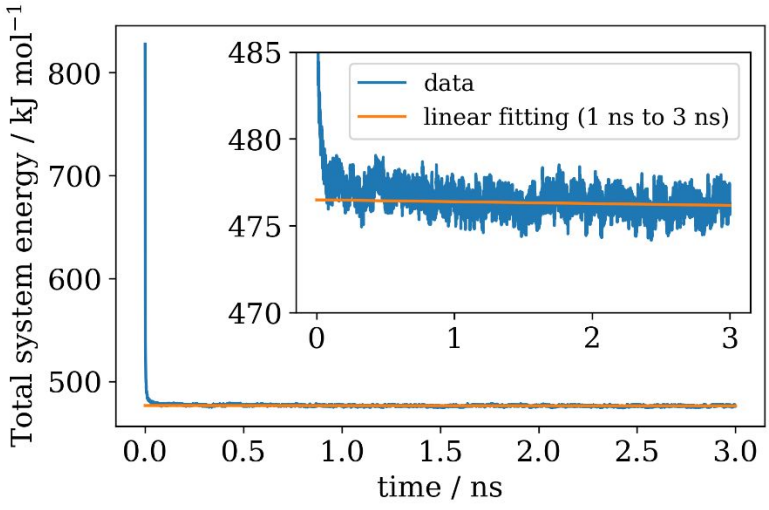

Figure. R1. Potential energy per ion in the MD cell as a function of time. The slope is −0.107±0.003 kJ mol^{-1} ns^{-1}.

As the referee pointed out, the number of ions in the system is an important information for readers. We added the

description in the revised manuscript as follows.

【before】 The initial configuration was made through bulk simulation, vacuum|liquid interface simulation, and equilibrated by uncharged graphene interface simulation.
【after】Page 2 The initial configuration was made through bulk simulation, vacuum|liquid interface simulation, and equilibrated by uncharged graphene interface simulation. The numbers of ion pairs in the system were 180, 360, and 360, respectively.

****

Referee: 2

Comments to the Author

The authors have addressed all comments in my previous review. I recommend publication of this manuscript as it is.

【Author reply】

We appreciate the referee's helpful review to enhance the quality of this manuscript.

PCCP

ARTICLE TYPE

Cite this: DOI: 00.0000/xxxxxxxxxx

Electric double layer structure and differential capacitance at the electrode interface of tributylmethylammonium bis(trifluoromethanesulfonyl)amide studied using molecular dynamics simulation.†

Seiji Katakura,[a] Naoya Nishi,*[a] Kazuya Kobayashi,[a] Ken-ichi Amano[a,b] and Tetsuo Sakka[a]

Received Date
Accepted Date

DOI: 00.0000/xxxxxxxxxx

A molecular dynamics simulation at the electrode interface of a quaternary ammonium ionic liquid, tributylmethylammonium bis(trifluoromethanesulfonyl)amide ($[N^+_{1444}][TFSA^-]$), has been performed. Unlike the commonly used cations, such as 1-alkyl-3-methylimidazolium and 1,1-alkylmethylpyrrolidinium cations, N^+_{1444} has multiple long-alkyl groups (three butyl groups). The behavior of ions at the electrode interface, especially these butyl groups has been investigated. N^+_{1444} at the first layer mainly has two types of orientations, lying and standing. The lying orientation is dominant at moderately negative potentials. However, the standing one becomes dominant at the more negative potentials. Due to this orientational change, the number of N^+_{1444} increases at the first layer as the potential becomes negative even at the potentials where the anions are completely depleted there. The change in orientation results in the upward deviation of the differential capacitance from the theoretical prediction at the negative potentials. The results suggest that the orientational preference caused by the steric constraint between alkyl groups plays an important role in the behavior of the electric double layer of the ionic liquids.

1 Introduction

Ionic liquids (ILs) are low-melting point salts that are only composed of ions. ILs have a wide potential window, high thermal stability, moderate ionic conductivity, and non-flammability. Since these properties are desirable to electrochemical materials, ILs have been applied to Li-ion batteries,[1] electric double layer capacitors,[2] fuel cells,[3] and many other electrochemical systems.[4] In these applications, chemical reactions and mass transfer at the interface between ILs and electrodes often play an important role. Hence, it is necessary to clarify the electric double layer (EDL) structure of ILs to understand and control these phenomena.

The EDL structure of ILs has been proposed to be unique due to excluded volume and local electrostatic interactions between ions.[5] In the case of dilute electrolyte solutions, conventional models such as the Gouy-Chapman model[6,7] can elucidate the EDL structure, without taking into account such interactions. However, the assumption of dilute solution is obviously inadequate for ILs because ILs themselves are solute ions and solvents. Kornyshev has proposed an EDL model for ILs[5] using a lattice gas model with mean-field approximation, which considers the excluded volume effect of ions as a local electrostatic interaction. Kornyshev's model predicts the potential dependence of the differential capacitance (C_d) for EDL of ILs. The predicted potential-C_d curve has a bell or camel shape depending on constituent ions: The bell shape curve has a maximum at the potential of zero charges (PZC), and the camel shape curve has two maxima at positive and negative potential sides of PZC. Recently, improved lattice gas models have also been proposed which consider the asymmetry of the ion size[8,9] and local electrostatic interaction between ions.[10,11] Molecular dynamics (MD) simulation studies[12–15] using all-atom models, which involves the geometric effect of the ions, have confirmed the camel and bell shape on the potential-C_d curve. Experimentally, the electrochemical impedance spectroscopy measurements[16–19] have also reported such behaviors. We have studied static (zero frequency) C_d using the pendant drop method,[20–22] which can avoid hysteresis[17,22–25] and the effect of slow relaxation[18,26–28] of the EDL structure, and succeeded in quantitatively analyzing the experimental potential-C_d curves with the lattice gas models.

[a] Address, Department of Energy and Hydrocarbon Chemistry, Graduate School of Engineering, Kyoto University, Kyoto 615-8510, Japan. Fax: 075 383 2490; Tel: 075 383 2491; E-mail: nishi.naoya.7e@kyoto-u.ac.jp
[b] Address, Faculty of Agriculture, Meijo University, Nagoya, Aichi 468-8502, Japan.

† Electronic Supplementary Information (ESI) available: [details of any supplementary information available should be included here]. See DOI: 10.1039/cXCP00000x/

The EDL characteristics of ILs have been revealed not only from macroscopic quantities such as C_d but also from the microscopic structure like the distribution and orientation of ions by using X-ray reflectometry (XR),[28–33] neutron reflectometry (NR),[34,35] atomic force microscope (AFM),[36,37] surface force apparatus (SFA),[38] scanning tunneling microscope (STM)[37,39] sum frequency generation (SFG),[40,41] surface enhanced infrared absorption spectroscopy (SEIRAS),[23,24] surface-enhanced Raman scattering (SERS),[42,43] and MD simulation.[12,15,44–49]

Quaternary ammonium-based ILs (QaILs) have a particularly wide potential window and therefore are desirable as electrolytes. Also, since a Qa cation has multiple alkyl groups, QaILs have more freedom in designing the ionic structure than imidazolium-based ILs. The EDL structure of QaILs has been rarely reported in contrary to the fact that many studies have been reported for the EDL structure of imidazolium-based ILs. Sharma and Kashyap[47] studied the EDL structure at the interface between QaILs and graphene electrode using triethyloctylammonium and (2-ethoxyethoxy)ethyltriethylammonium as constituent cations and bis(trifluoromethansulfonyl)amide ($TFSA^-$) as the common anion using MD simulation. Substituting alkyl group with diether group, the authors found the change in the EDL structure, such as an increase in the parallel orientation of the longest tail near the electrode for the diether one compared to the alkyl one. They also studied EDL structure and the electrostatic properties of pyrrolidinium-based ILs, which have quaternary ammonium and cyclic structure, with focusing on the role of linear and nonlinear alkyl tails.[48,49] We have previously studied the EDL structure at the interface between QaILs and gold electrode using SEIRAS[50] and elucidated that the behavior of Qa cations in the EDL is affected not only by the length of alkyl chain in Qa cations but also by that of the perfluoroalkyl chain in the anion. Moreover, we have studied the dynamics of the EDL structure of QaILs using electrochemical surface plasmon resonance (ESPR)[27,51] and revealed the ultra-slow dynamics on the order of minutes. We also investigated the surface structure of QaILs by using XR[52,53] and found the spontaneous formation of ionic multilayers. We performed MD at the interface between QaILs and vacuum[54] and clarified the effect of the number of long alkyl chains in Qa cation on the interfacial structure. Nevertheless, the EDL structure of QaILs is hardly elucidated at present, and therefore, the potential dependence of orientations and distributions of ions should be clarified.

In the present study, we studied the EDL structure of tributylmethylammonium $TFSA^-$ ($[N^+_{1444}][TFSA^-]$) at the molecular level by using MD simulation. N^+_{1444} has a three-dimensional structure in which three butyl groups surround the polar part. Since such bulky non-polar parts lead to complicated steric constraint between neighboring cations in EDL, they play an important role in the EDL structure. Therefore, we evaluated the EDL structure by focusing on the behavior of both the polar parts and butyl chains at the first layer.

2 Methods

2.1 Computational detail

MD simulation at the interface of $[N^+_{1444}][TFSA^-]$ | graphene electrode was performed using DL_POLY classic.[55] The structure of $[N^+_{1444}][TFSA^-]$ and the definitions of atomic names are shown in Fig. 1.

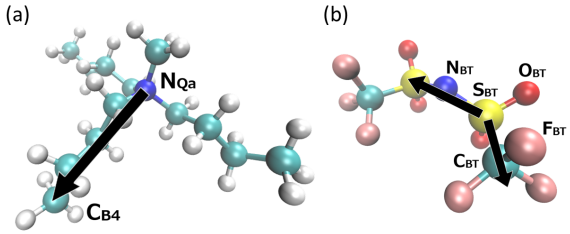

Fig. 1 Structure of (a) N^+_{1444} and (b) $TFSA^-$, and definitions of intramolecular vector to calculate the orientations of ions. N_{Qa} and N_{BT} are assumed as a representative of polar-part of N^+_{1444} and $TFSA^-$. C_{B4} is assumed as that of nonpolar-part of N^+_{1444}.

We used an all-atom force field, CL&P,[56] for $[N^+_{1444}][TFSA^-]$. The specific parameters are described elsewhere.[54] For the force field of the graphene carbon atoms, we used the van der Walls parameter of the sp_2 carbon atom from OPLS AA.[57] We set the surface charge density of the graphene σ_{elec} by evenly allocating the charge to each carbon atom constituting graphene. The cutoff distance of the vdW force was 10 Å. For the calculation of long-range force, three-dimensional smooth particle mesh Ewald method[58] (SPME) was used with an accuracy of 10^{-5}, and the real space cutoff was set to 10 Å. In order to take electronic polarization into account,[59,60] the electrostatic interaction was scaled with relative permittivity $\varepsilon_r = 2$.[54,61] No slab correction for 3-dimensional periodicity was used. Although it is desirable to include slab correction, the presence or absence of slab correction did not cause any serious problem on the discussion made in the present study. We examined the effect of the correction and found that the interfacial potential difference in the present study was lower than that with the correction (see Fig. S3). This is consistent with a previous MD study[15] that compared the effect of slab correction.

The same initial configuration of the interface between $[N^+_{1444}][TFSA^-]$ and graphene was used for all the charged conditions. The initial configuration was made through bulk simulation, vacuum|liquid interface simulation, and equilibrated by uncharged graphene interface simulation. The numbers of ion pairs in the system were 180, 360, and 360, respectively. The procedure of bulk simulation and vacuum|liquid Maninterface simulation was described elsewhere.[54] Orthorhombic MD cells (Fig. 2), were used for the interface simulations with geometries (l_x, l_y, l_z), where l_x, l_y, and l_z are the side lengths in x-, y-, and z-direction, respectively. The cell has a ~100 Å thick IL slab confined by electrodes and ~200 Å thick vacuum. The l_x and l_y ($l_x = l_y = 49.9635$ Å) of the equilibrium configuration of the gas-liquid interface were slightly expanded to (l_x, l_y) = (51.6852 Å, 51.1560 Å), which correspond to an integral multiple of the unit

cell of graphene sheet. Then two graphene sheets were put at the vacuum phase near the interfaces at the positive side and negative side of z. Then the positions of the graphene sheets were adjusted and fixed so that the cavity between the sheet and IL disappeared. Even after the disappearance of cavities, the IL density is low. Hence, the configuration was compressed in the z-direction so that the further calculation gives the same density at the IL bulk region as the vacuum-liquid interface MD in our previous study[54](see Fig. S1). In the compressed configuration, the distance between the two graphene electrodes was 103.1 Å. From this configuration, a calculation was performed for 3 ns to obtain the configuration which is used as a common initial configuration for different σ_{elec}.

Starting from this initial configuration, a set of electrode interface MD calculations was performed by changing σ_{elec}. Charges were equally distributed to the each carbon atom of electrode to give $\pm$ σ_{elec} for each electrode. Then 3 ns calculation was performed. The first 1 ns was regarded as an equilibration process, and the remaining 2 ns was used for data analysis. The geometry of this MD cell was (l_x, l_y, l_z) = (51.6852 Å, 51.1560 Å, 300.0000 Å) (See Fig. 2). The $|\sigma_{\mathrm{elec}}|$values were varied as a minimum unit with 1.01 μC/cm^2 in the range from 0 to 12.11 μC/cm^2, and 3.03 μC/cm^2 in the range from 12.11 to 36.36 μC/cm^2. The MD simulation was performed in the NVT ensemble. The time step was 2 fs in all cases. The temperature was controlled at 423 K using a Berendsen thermostat.[62] Although the Berendsen thermostat may cause artificial collective motion[63] in some simulation systems and therefore the use of other thermostats[64–66] is preferred, we did not observe such an artificial motion of ions.

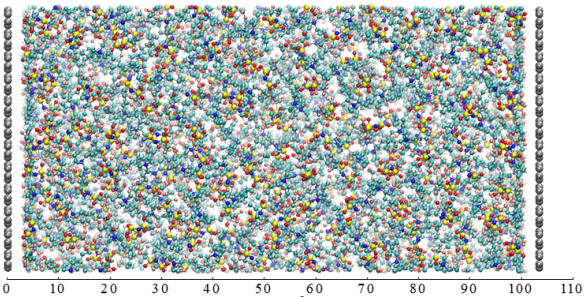

Fig. 2 Geometry of the MD cell.

2.2 Data analysis

MD trajectories were analyzed to produce number density distributions $\rho_{\mathrm{i}}(z)$ for each atom i as a function of z, the distance from the electrode (the center of the graphene C atom). We regarded the N atoms of N^+_{1444} and $TFSA^-$ (N_{Qa} and N_{BT} respectively, see Fig. 1) as representative points of the polar part of each ion, and C atoms at the end of the butyl chains (C_{B4}) as those of non-polar part. To investigate changes in the composition of the first layer at the interface, we calculated surface densities Γ of atoms i there (i = N_{Qa}, N_{BT}, and C_{B4}) by integrating the first peak of the number density distributions as follows.

$$\Gamma_{\mathrm{i}} = \int_0^{z_{\mathrm{div}}} \rho_{\mathrm{i}} \mathrm{d}z \tag{1}$$

The upper limit of the integration (z_{div}) for N_{Qa}, N_{BT}, and C_{B4} were set to be 6.55, 6.45, and 6.95 Å, respectively, which were determined to cover the first peak of ρ_{i} for all σ_{elec} conditions.

The orientational distributions $p_{\mathrm{i\text{-}j}}(\theta)$ of the intramolecular vectors from atom i to j (i-j = N_{Qa}-C_{B4}, S_{BT}-S_{BT} and S_{BT}-C_{BT}, see Fig. 1 for the definitions) in the first layer were calculated. $p_{\mathrm{i\text{-}j}}(\theta)$ is defined so that it satisfies

$$\int_0^{2\pi}\int_0^{\pi} p_{\mathrm{i\text{-}j}}(\theta,\psi)\sin\theta \mathrm{d}\theta\mathrm{d}\psi = 4\pi. \tag{2}$$

Here, θ is the angle between the intramolecular vector and the z axis, i.e. polar angle, and ψ is the azimuthal angle. Since the assumption that $p_{\mathrm{i\text{-}j}}(\theta,\ \psi)$ does not depend on ψ is reasonable (see Fig. S2), the eq. (2) can be integrated over ψ, as follows,

$$\int_0^{\pi} p_{\mathrm{i\text{-}j}}(\theta)\sin\theta \mathrm{d}\theta = 2 \tag{3}$$

If an intramolecular vector have an isotopic distribution as in bulk, then $p_{\mathrm{i\text{-}j}}(\theta) = 1$ for any value of θ. Note that $p(\theta)$ is not a population distribution function but a probability density function. To determine if an ion is at the first layer, the z position of N atom of N^+_{1444} and $TFSA^-$ (N_{Qa} and N_{BT}) was compared with z_{div}. Therefore, one can obtain the population of the vector i-j at θ by multiplying $p(\theta)$ with $\sin\theta$, which is the contribution of solid angle, and Γ_{i}. Because of the structure of the ions, three different intramolecular vectors of N_{Qa}-C_{B4} can be defined for each ion. Their three θ were calculated independently, and then averaged as $p_{\mathrm{i\text{-}j}}(\theta)$. Two different intramolecular vectors of S_{BT}-S_{BT}, and S_{BT}-C_{BT} were treated in the same way.

In order to investigate the in-plane structure of the first layer, the two-dimensional radial distribution functions for N_{Qa}-N_{Qa} and N_{BT}-N_{BT} in the layer were calculated. Here, the two-dimensional radial distribution function $g_{xy,\mathrm{i}}$ is expressed by the following equation.

$$g_{xy,\mathrm{i}}(r_{xy}) = \frac{\Delta n_{\mathrm{i}}(r_{xy})}{2\pi r \Delta r_{xy}\rho_{\mathrm{surf}}} \tag{4}$$

where, r_{xy} is the projected distance between two i atoms onto the xy plane, and $\Delta n_{\mathrm{i}}(r_{xy})$ is the number of atoms i present from r_{xy} to $r_{xy}+\Delta r_{xy}$, and ρ_{surf} is the surface density of atom i in the first layer.

Charge density distribution $\rho_{\mathrm{chg}}(z) = \sum_i \rho_{\mathrm{i}}(z)q_{\mathrm{i}}$, where q_{i} is a partial charge of the atom i, was calculated and converted into the potential distribution profile $\phi(z)$ (See Fig. S4) using the Poisson equation. The one-dimensional Poisson equation is as follows

$$\frac{\mathrm{d}^2}{\mathrm{d}z^2}\phi = -\frac{\rho_{\mathrm{chg}}}{\varepsilon_0\varepsilon_{\mathrm{r}}} \tag{5}$$

where ε_0 is the dielectric constant of vacuum and ε_{r} = 2 is the relative permittivity. Since SPME was used without using a slab correction, the "tin foil boundary condition" has been established, which means the potentials at both sides of periodic boundaries for each direction of the MD cell should be the same. There-

fore, the first integral constant for the Poisson equation was determined to satisfy the condition for the boundary in z-direction. The second integration constant was determined to set the potential in the IL bulk (ϕ_{bulk}) to be 0. Here, ϕ_{bulk} was obtained by averaging the electric potential in the range of ± 20 Å from the middle (z_{cent}) of the z coordinate of the two electrodes. Since $\phi_{\mathrm{bulk}} = 0$, the potential at the electrode ($z = 0$) represents the interfacial potential difference ($\Delta\phi = \phi_{\mathrm{elec}} - \phi_{\mathrm{bulk}}$).

The differential capacitance C_{d} for each potential were calculated by numerically differentiating the surface charge density σ_{elec} of the electrode with respect to $\Delta\phi$ as shown in the following formula.

$$C_{\mathrm{d}} = \frac{\mathrm{d}\sigma_{\mathrm{elec}}}{\mathrm{d}\Delta\phi} \tag{6}$$

For the numerical differentiation of eq. (6), quadratic regression was applied for each five consecutive points in the σ_{elec}-$\Delta\phi$ plot shown in Fig. S3. Four consecutive points were used for the second potential from the edge (-8.3 V and 5.1 V) in Fig. S3.

3 Results and Discussions

3.1 Number density distributions

The number density distributions as a function of the distance from the electrode (z) are shown in Fig. 3 (a)-(e), for N atom in N^+_{1444} (N_{Qa}), and C atoms at the end of butyl groups in N^+_{1444} (C_{B4}), and N atom in $TFSA^-$ (N_{BT}). All of these number density distributions showed oscillation which attenuated from the interface to the bulk. The oscillation of the N_{Qa} and N_{BT} were almost in phase when the electrode was not charged (Fig. 3 (c)), but were out of phase when the electrode was charged (Fig. 3 (a), (b), (d), and (e)). When the electrode is positively charged (Fig. 3 (a) and (b)), the odd- and even-number-th layers were composed of $TFSA^-$ and N^+_{1444}, respectively, and the order was reversed when the electrode was negatively charged. These results are consistent with previous studies by XR[25,29] and MD[25,44] for other types of ILs and an MD study for QaILs.[47] These results at relatively less charged interface also consistent with our previous studies[67,68] using integral equation theory.

To understand the gradual change in number density distributions at different potentials, their contour maps are also shown in Fig. 3 (f), (g), and (h) for N_{Qa}, N_{BT}, C_{B4}, respectively, with being normalized by the bulk density. All of these number density distributions at any potentials showed particularly sharp peaks either or both at $z \sim 4$ and ~ 8 Å, corresponding to the first and second layer, respectively. Since the peak at $z \sim 4$ Å for these atoms did not show large shift, we were able to define the boundary between the layers (z_{div}) for N_{Qa}, C_{B4}, N_{BT} as 6.55, 6.45, 6.95 Å, respectively. The boundaries are shown as the vertical dotted lines in Fig. 3 (f), (g), and (h). These values were determined to cover the first peak for all σ_{elec} conditions as described in the data analysis section.

First, we focus on the amplitude of the oscillation of N_{Qa} and N_{BT} (Fig. 3 (f) and (g)). As already shown in Fig. 3 (a) and (b), N_{Qa} forms the second ionic layer ($z \sim 8$ Å) at positive potentials, while N_{BT} forms the first ionic layer ($z \sim 4$ Å). It was reversed on the negative potentials. The peaks at $z \sim 8$ Å for N_{BT} and at $z \sim 13$ Å for N_{Qa} were highest at -2 V, which means alternating cation and anion layers are predominant at the potential, as exemplified in Fig. 3 (d). When the potential became more negative than -2 V, the amplitude of the oscillation decreased. The oscillation in Fig. 3 (f) and (g) becomes the smallest on the negative potentials at -5.4 V, which corresponds to Fig. 3 (e). In Fig. 3 (e), the number density distribution of N_{Qa} atoms showed a small peak in the second layer ($z \sim 8$ Å) next to the big first layer peak, indicating the negative charge on the electrode beyond the limit of charge compensation by the first ionic layer. In other words, the first layer is saturated with cations. The development of second ionic layer by the cation at the more negative potentials in Fig. 3 (f) is a result of the saturation.

Such saturation is called "crowding" and has been revealed by MD[44,69] and theory[70] for the EDL in ILs. The present result in negative potentials agrees with the previous MD studies.[44,69] In the positive potentials, the "crowding" of $TFSA^-$ was not observed because the potentials are not positive enough. According to one of the previous studies,[69] the crowding is accomplished by the larger surface charge density of the electrode for the smaller IL ions. We compared the molecular volumes of N^+_{1444} and $TFSA^-$ from DFT calculations at B3LYP/6-311++G(d,p) level using Gaussian 09W.[71] The volume of $TFSA^-$ (128 $\mathrm{cm^3\ mol^{-1}}$) was smaller than that of N^+_{1444} (205 $\mathrm{cm^3\ mol^{-1}}$). The small size of $TFSA^-$ will be the reason why the crowding of $TFSA^-$ was not observed within the σ_{elec} (potential) range studied.

Next, we focus on peak shifts depending on the potential in Fig. 3 (f) and (g). In Fig. 3 (f), the first ionic layer of N_{Qa} ($z \sim 4$ Å) showed peak shift only slightly, which implies that the orientation change of N^+_{1444} has little effect on the distance of the polar part of N^+_{1444} from the electrode. Conversely, in Fig. 3 (g), the first ionic layer of N_{BT} shifted particularly at $\Delta\phi \sim 0$ V, implying that the orientational change of $TFSA^-$ in the first ionic layer is accompanied by the change in the distance of the polar part of $TFSA^-$. The orientation of ions in the first ionic layer will be discussed in the later section in detail.

The peak shifts of the second ionic layer ($z \sim 8$ Å) were also observed. Specifically, the peak of the second ionic layer for N_{Qa} at positive potentials and N_{BT} at negative potentials shifted toward the IL bulk phase with increasing $|\Delta\phi|$, indicating the increase in the effective thickness of the first ionic layer. The shifts can also be clearly observed in Fig. 3 (a)-(d), by comparing (a) with (b) and (d) with (e). The peak shift at positive potentials was related to the behavior of C_{B4}. In Fig. 3 (b), the first layer peak can be observed for C_{B4} but not for N_{Qa}. Therefore the C_{B4} in the first layer should belong to N^+_{1444} whose N_{Qa} is located at the second layer. This "interlayer crossing" of butyl chain was observed not only from the second to the first layer (Fig. 4 (c)) but also vice versa (Fig. 4 (a)). The N^+_{1444} without the interlayer crossing are also shown in Fig. 4 (b) and (d). Although all the snapshots were taken from the uncharged interface, these were the typical orientations of N^+_{1444} for all the potentials.

MD studies[44,69] for the EDL of ILs using Lennard-Jones sphere model also demonstrated the shift of the ionic layer in the same direction as described above. Compared to these previous studies, a notable characteristic in the present study is the difference in peak shifts between the cation and anion: almost stable peak

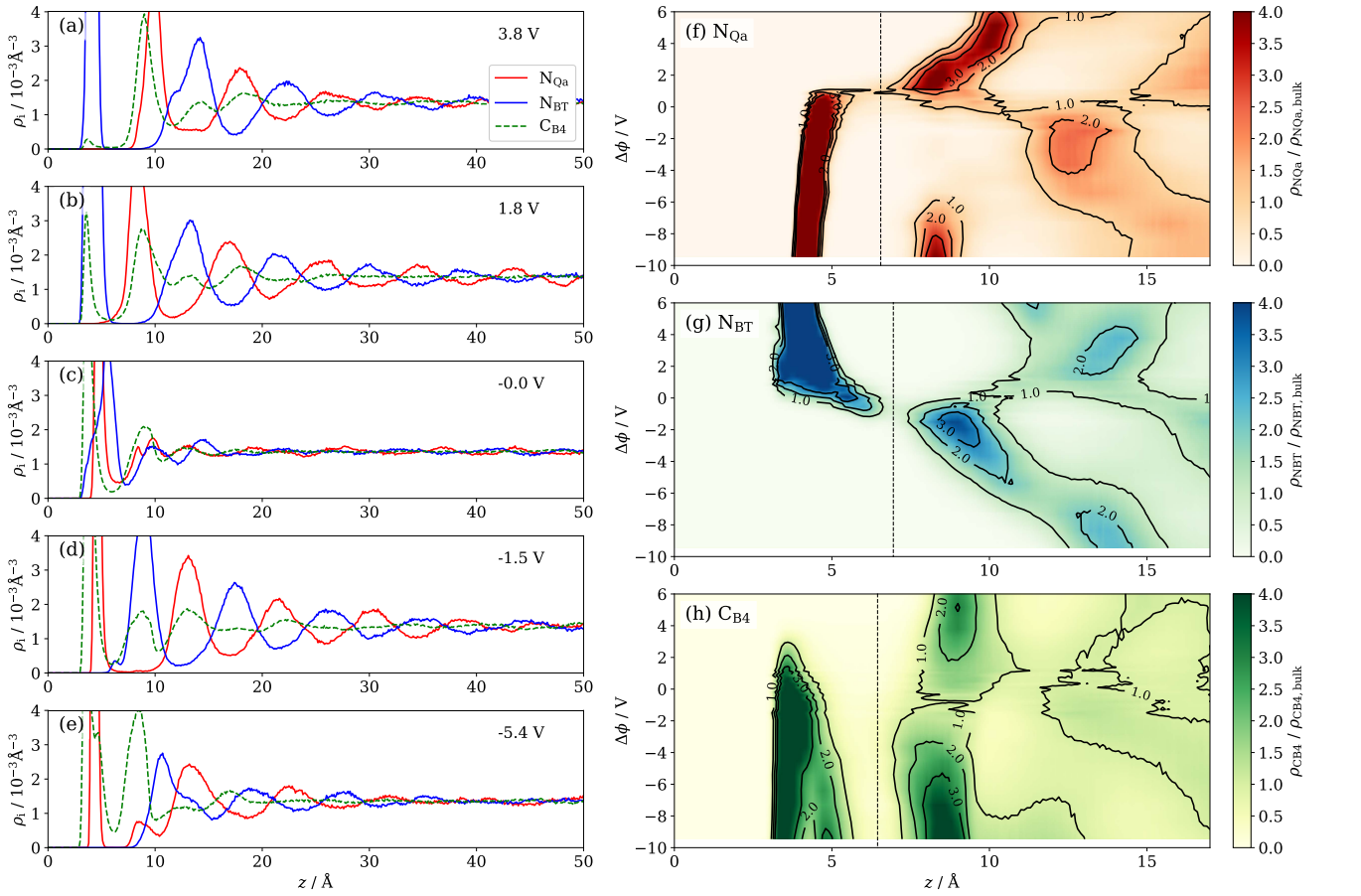

Fig. 3 Number density distributions ρ_i (red; N_{Qa}, blue; N_{BT}, green; C_{B4}) at different potentials ((a)-(e)) and the potential dependence of normalized ρ_i illustrated in contour maps in z-$\Delta\phi$ plane ((f)-(h)). The black vertical dotted lines are the boundary between the first layer and the second layer (z_{div}) for each atom.

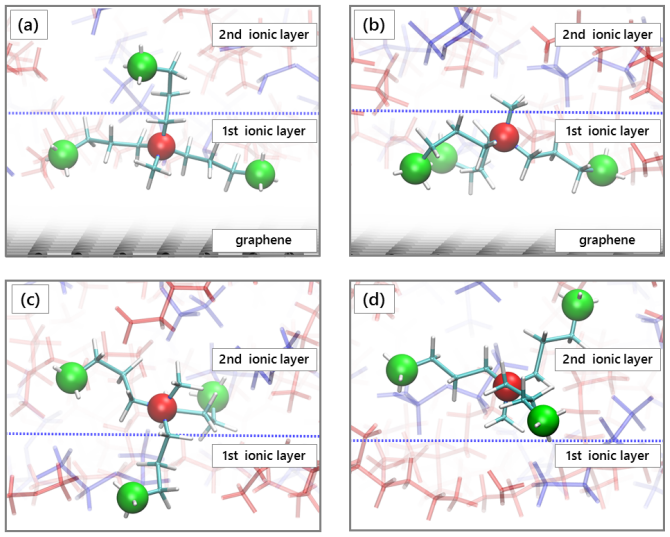

Fig. 4 Side-view snapshots of N^+_{1444}. The electrode is located at the bottom of each figure. (a): N^+_{1444} at the first layer with one butyl group crossing to the second layer (one butyl group perpendicular to and two butyl groups parallel to the electrode). (b): N^+_{1444} at the first layer without crossing to the second layer(all the three butyl groups parallel to the electrode). (c): N^+_{1444} at the second layer with one butyl group crossing to the first layer. (d): N^+_{1444} at the second layer without crossing to the first layer.

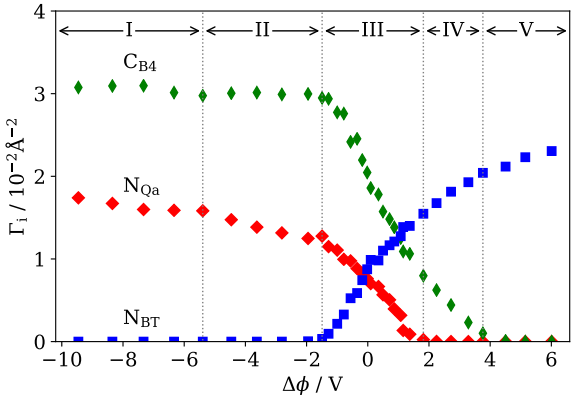

Fig. 5 Surface density of the portion of ions at the first layer (Γ_i; i = N_{Qa} (red), N_{BT} (blue), C_{B4} (green)). The range of the first layer (z = 0 to z_{div}) are shown in Fig. 3(f)-(h). The vertical dotted lines are the potential boundary where the behavior of the Γ_i has changed. I: N^+_{1444} is almost saturated. II: there is still no $TFSA^-$. III: N^+_{1444} and $TFSA^-$ are mixed. IV: the polar part of N^+_{1444} is absent, but the butyl group is still in the first layer. V: the whole part of N^+_{1444} is absent.

position for N_{Qa} and shift for N_{BT} for the first layer, which are the effects of the geometry of polyatomic ions. The former reflects that the closest distance between N_{Qa} and electrode in Fig. 4 (a) and (b) are almost the same. The latter reflects that the closest distance between N_{BT} and electrode depends on the orientation of $TFSA^+$, which will be shown later. Regarding second layer, the dramatic shift for N_{Qa} around 4 V reflects the depletion of the butyl group crossing to the first layer. On the other hand, the gradual shift for N_{BT} at $\Delta\phi \sim 0$ to ~ -6 V reflects the gradual crowding of the butyl group at the first and second layers.

3.2 Composition of first ionic layer

We analyzed the surface density Γ of N_{Qa}, C_{B4}, N_{BT} at the first ionic layer to investigate the change in the composition of the first ionic layer (Fig. 5). As described in the Data analysis section, the Γ values were calculated by integrating the first layer peaks in the number density distribution profiles. Here, note that the ratio of Γ_{CB4} on Γ_{NQa} is not always coincident with three, which is the stoichiometric ratio in a N^+_{1444} cation. This discrepancy is due to independent belongings of N_{Qa} and C_{B4} to layers in the present study. The snapshots are shown in Fig. 4 (a), (b), (c), and (d). In Fig. 4 (a), for example, a C_{B4} atom of an N^+_{1444} is located at the second layer region (z $\sim$ 8 Å) and the N_{Qa} atom of the same N^+_{1444} belongs to the first ionic layer, and therefore the C_{B4} atom is counted as the portion of the second layer.

We focus on the behavior of Γ_i at negative potentials $\Delta\phi = 0$ to -10 V. The potentials can be separated into three regions, which are shown in Fig. 5 as region III, II, and I. First, in the potential region III, as the potential becomes more negative, the increases in Γ_{NQa} and Γ_{CB4}, and the decrease in Γ_{NBT} occurred simultaneously. Second, the III/II boundary is defined as the potential at which N_{BT} disappears from the first ionic layer. In region II, the increasing rate of Γ_{NQa} becomes slower than that in region III. Moreover, Γ_{CB4} is constant in the region II. Third, the II/I boundary is defined as the potential at which Γ_{NQa} becomes constant, and N^+_{1444} starts to form the second ionic layer. In region I, the increase in the number of N^+_{1444} occurs in the second ionic layer rather than the first ionic layer, although one can still see a slight increase in Γ_{NQa}. This phenomenon is the so-called ion crowding, as described before. It is interesting that the behaviors of Γ_{NQa} and Γ_{CB4} are different, which implies the change in the orientation of N^+_{1444}.

We focus on the positive charging process in Fig. 5 from $\Delta\phi = 0$ to 6 V. The III/IV and IV/V boundaries were determined at the potentials at which Γ_{NQa} and Γ_{CB4} become almost zero, respectively. In the whole regions from $\Delta\phi = 0$ to +6 V, Γ_{NBT} increased, but the rate decreased as the potential becomes positive. In region V, there is no butyl chain in the first ionic layer. In spite of the absence of the butyl chain, which decreased along with the increase in Γ_{NBT} in region IV, Γ_{NBT} still increased as the potential becomes more positive in region V. It is likely that cavities between $TFSA^-$ are being filled and well-packed $TFSA^-$ layer is being formed in region V.

3.3 Orientational distribution of butyl chain in N^+_{1444}

The orientational distributions of butyl chain in N^+_{1444}, $p_{NQa\text{-}CB4}(\theta)$, and snapshots of N^+_{1444} at the first ionic layer are shown in Fig. 6. The dependence of $p_{NQa\text{-}CB4}(\theta)$ on the potential is also shown in Fig. S5 as a contour map.

The $p_{NQa\text{-}CB4}(\theta)$ profiles mainly had two peaks for all the potentials: One was a sharp peak at $\theta \sim 100°$, and the other was a broad peak from 0° to 70°. The two peaks indicate that the three butyl chains in N^+_{1444} have two orientational preference. The sharp peak corresponds to the orientation in which a butyl

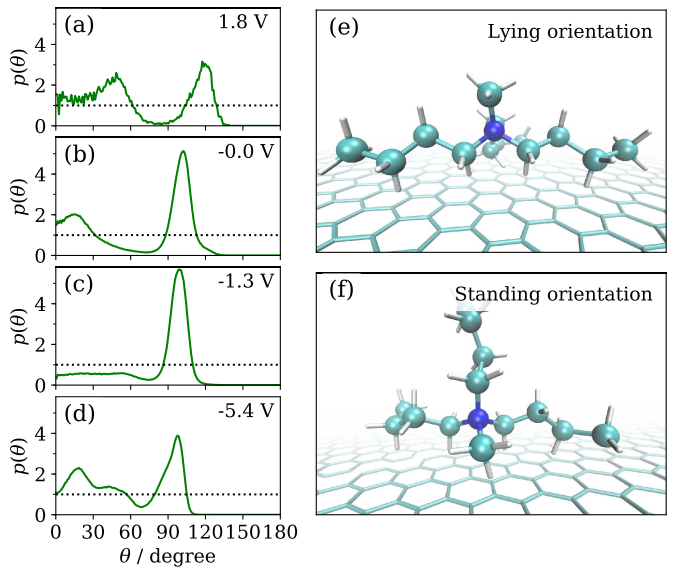

Fig. 6 (a)-(d): Orientational distribution function $p_{NQa-CB4}(\theta)$ of the intramolecular vector N_{Qa}-C_{B4} of N^+_{1444}. (e), (f): Lying and standing orientations of N^+_{1444} in the first layer. The broad peak from 0° to 70° in (a)-(d) corresponds to the butyl group perpendicular to the electrode only appearing in the snapshot (f), whereas the sharp peak at 110° corresponds to those parallel to the electrode appearing in both (e) and (f).

chains is relatively parallel to the electrode. In Fig. 6 (e), all the three butyl chains in N^+_{1444} have this orientation. In the present study, we refer to such orientation of N^+_{1444} in Fig. 6 (e) as "lying orientation." On the other hand, the broad peak in Fig. 6 corresponds to the orientation in which the butyl chain is relatively perpendicular to the electrode. As Fig. 6 (a)-(d) show, the broad peak shifted and splitted depending on the potential, indicating that the peak includes some orientations of the butyl chain. In the present study, we regarded them as the same group of orientation. The snapshot in Fig. 6 (f) is a typical orientation of N^+_{1444} in which one of the butyl chains is relatively perpendicular to the electrode. In the present study, we refer to the orientation of N^+_{1444} as "standing orientation." The snapshot shows that one of the butyl chains stands, but the other two lie in the standing orientation. Therefore, it should be noted that these two orientations of N^+_{1444} do not correspond one-by-one to the two peaks in $p_{NQa-CB4}(\theta)$. It should also be noted that the orientations of butyl chains in a N^+_{1444} are not independent, because they are covalently bonded to the quaternary N atom. This effect was observed as the peak split in Fig. 6 (d). One of the peaks ($\theta \sim 50°$) corresponds to the standing orientation of N^+_{1444} in which two butyl chains stand. Because of mutual exclusion between chains, the orientational angles of standing two butyl chains tend to be larger than that of the one butyl chain standing case as in Fig. 6 (f).

Interestingly, at −1.3 V (Fig. 6 (c)), the "lying" peak of $p_{NQa-CB4}(\theta)$ is the sharpest whereas the "standing" peak is obscure, indicating that the lying orientation of N^+_{1444} is the most predominant at this potential. The standing orientation becomes competitive at the positive potential side or further negative potential (Fig. 7).

3.4 Fraction of orientations of butyl chains

Since Fig. 6 revealed two preferred orientations of butyl chains in N^+_{1444}, we investigate the fraction of these orientations as a function of the potential. To calculate the fraction, we integrated $p_{NQa-CB4}(\theta)$ for θ ranges corresponding to the orientations using eq. (3) and divided by two.

The ranges of θ were from 0° to θ_{div}, and θ_{div} to 180°, where θ_{div} was the orientational angle where $p_{NQa-CB4}(\theta)$ showed the local minimum around $\theta \sim 60°$. The fraction of orientations of butyl chains is shown in Fig. 7 as a function of the potential. The purple plots for the "standing" peak indirectly reflect the amount of standing orientation of N^+_{1444}. Note that the green plots for the "lying" peak reflect both of the standing and lying orientations of N^+_{1444} (Fig. 6 (e) and (f)), but can be an index of the fraction of the lying orientation. The sum of these plots is one for all the potential, which can be easily checked from eq. (3).

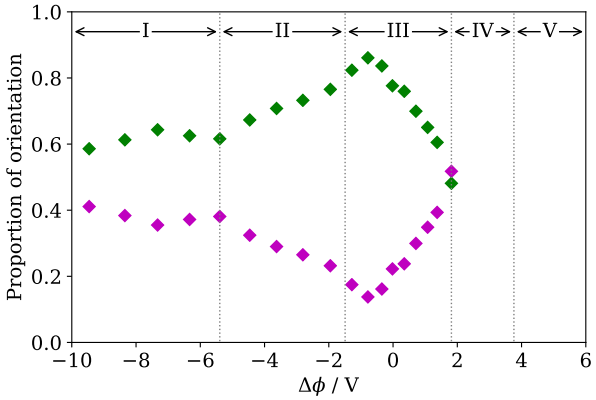

Fig. 7 Fraction of butyl group standing (purple) and lying (green) in the first interface layer. The fraction was calculated by integrating the two peaks in $p_{NQa-CB4}(\theta)$ shown in Fig. 6 based on eq. (3). The marked regions I-V correspond to Fig. 5.

Fig. 7 showed that the fraction of the lying orientation is highest at a negative potential in the potential region III, decreases as the potential becomes more negative in the region II, and is almost constant at the region I.The potential dependence of the fraction of orientations agrees with that of the composition of the first ionic layer (Fig. 5), which was described above.

First, in region III, the fraction of lying orientation increases as the potential becomes more negative, which is likely to contribute to the higher increase rate of Γ_{CB4} than that of Γ_{NQa} in the same region(Fig. 5). Note that the interpretation is not simple because the depletion of N^+_{1444} at the second layer also contributes to the decrease in Γ_{CB4} (See Fig. 4 (c)). Second, in the region II, the lying orientation decreased, although Γ_{CB4} was almost constant(see Fig. 5). Probably the contribution of orientation was compensated by the increase in the number of N^+_{1444} at the first layer, which was observed as the increase in Γ_{NQa}. In other words, the change in the orientation permits the increase in the number of N^+_{1444} in the first layer at the potentials where $TFSA^-$ is absent. The almost constant fraction of the orientation in region I also agrees with the saturation of Γ_{NQa} and development of cationic second layer. In region I, N^+_{1444} is likely to be in the optimal ori-

entation to be fully packed in the first ionic layer.

This orientational behavior may indicate that N^+_{1444} tends to lie the butyl chains with satisfying the number of the cation required by the electroneutrality. This trend can be explained by Asakura-Oosawa theory,[72] for the depletion force between large particles in liquids. When a liquid mixture is composed of large and small molecules, the theory predicts that large molecules prefer to be in contact with solid substrate because of the overlap of excluded volumes of the large molecule and the substrate.[73,74] Although the contact causes a loss of translational entropy of the large molecule, it increases available space for small molecules to move and leads to the gain of their translational entropy, leading to the increase in the total entropy of the system. In the present study, the N^+_{1444} in the lying orientation makes more ions freely translate and therefore, entropically preferable.

The change in orientation of N^+_{1444} affects the electrostatic interaction with neighboring ions as well. The standing butyl chains at positive potentials in region III, where the anions are dominant in the first ionic layer, indicate shorter distance with neighboring anions and stronger in-plane attractive interaction. On the other hand, the lying butyl chains at negative potentials in region III, where oppositely the cations are dominant, implies weaker in-plane repulsive electrostatic interaction with neighboring cations and stronger out-of-plane attractive interaction with anions existing in the second ionic layer. The increase in the proportion of standing butyl chains with decreasing the potential in region II indicates the shorter distance with cations in the in-plane direction and longer distance with anions in the out-of-plane direction, both of which are not energetically preferable but are compensated for by the strong attractive interaction between cations and negative charge on the electrode surface.

3.5 Orientation distribution of $TFSA^-$

To understand the behavior of ions in the first ionic layer the orientations of $TFSA^-$ as well as N^+_{1444} is important. We calculated $p_{\text{i-j}}(\theta)$ of the intra-molecule vectors of $TFSA^-$ in the first ionic layer. The $p_{\text{i-j}}(\theta)$ of S_{BT}-S_{BT} and S_{BT}-C_{BT} are shown in Fig. 8 (a) and (b), respectively, as contour maps as a function of potential and θ.

Here we focus on the behavior in the positive potentials. The peak of $p_{\text{SBT-SBT}}(\theta)$ at $\theta \sim 90°$ increased with increasing the potential, indicating the increase in the orientation of S_{BT}-S_{BT} vector parallel to the electrode. At the same time, the peak of $p_{\text{SBT-CBT}}(\theta)$ at $\theta \sim 90°$ decreased, and that at $\theta \sim 30°$ increased, indicating that the increase in the number of CF_3 groups pointing to the IL bulk. These peaks of $p_{\text{SBT-SBT}}(\theta)$ and $p_{\text{SBT-CBT}}(\theta)$ correspond to the orientation of $TFSA^-$ shown in Fig. 8 (c) and (d). At the positive potentials in regions IV and V, the orientation in Fig. 8 (c) is superior to that in Fig. 8 (d). The orientation of $TFSA^-$ in Fig. 8 (c) occupies a large area on the electrode than the orientation in which the S_{BT}-S_{BT} vector stands. One may expect that $TFSA^-$ stands at the positive potentials, like Fig. 8 (e), similarly to the orientational behavior of N^+_{1444}, in which more N^+_{1444} showed standing orientation as potential become negative. However, such standing orientation of $TFSA^-$ was less observed as the

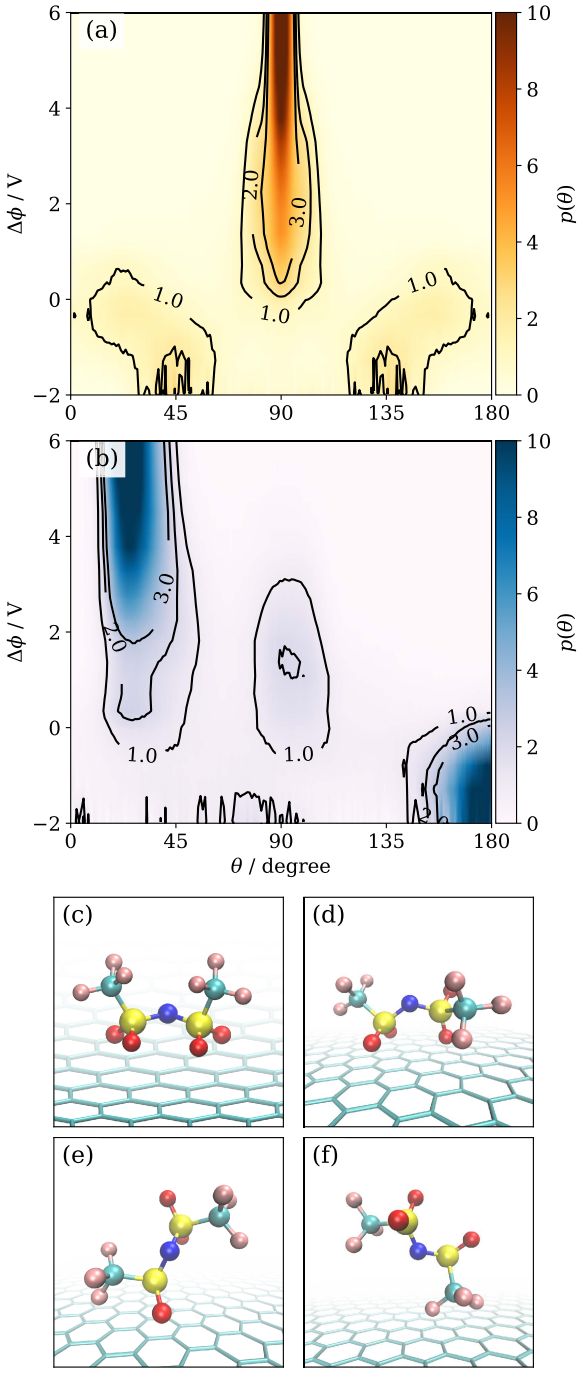

Fig. 8 (a), (b): Contour map of $p_{\text{SBT-SBT}}(\theta)$ (a) and $p_{\text{SBT-CBT}}$ (b) on the $\Delta\phi$-θ plane. (c)-(f): Snapshots of $TFSA^-$ in the first ion layer. In the order of (c)> (d)> (e)> (f), the fraction of the $TFSA^-$'s orientation increases as the potential becomes positive.

potential becomes positive, probably because the standing orientation increases the distance between the electrode and polar-part of $TFSA^-$ (N_{BT} and O_{BT}), which is electrostatically unstable. Furthermore, ions in standing orientation have a loss of entropy compared with that in lying orientation as already discussed with Asakura-Oosawa theory. The standing orientation would permit the larger number of $TFSA^-$ in the first ionic layer, but it does not cause energetic and entropic advantage, unlike the N^+_{1444} case. On the other hand, CF_3 group standing at positive potentials is similar to the orientational behavior of N^+_{1444}.

Next, we focus on negative potentials in Fig. 8. The orientational preferences of $TFSA^-$ were different from those in positive potentials. In Fig. 8 (a), the broad peaks in $p_{\text{SBT-SBT}}(\theta)$ at $\theta \sim 0°$ to $60°$ and $\theta \sim 120°$ to $180°$ were observed, indicating that the vector is standing rather than lying on the electrode. At the same time, for $p_{\text{CBT-SBT}}$ (Fig. 8 (b)) the peak at $\theta \sim 180°$ increased as the potential becomes more negative, indicating that the CF_3 group in $TFSA^-$ points to electrode. When S_{BT}-S_{BT} is relatively standing, a CF_3 group touches the electrode, whereas the other CF_3 group in the same $TFSA^-$ should depart from the surface of the electrode. The orientations of $TFSA^-$ at negative potentials are shown in Fig. 8 (e) and (f). The fraction of Fig. 8 (f) orientation increases as the potential becomes more negative. The drastic change in the orientational preference from positive to negative potential also agreed with the peak shift of the first ionic layer shown in number density distribution of N_{BT} in Fig. 3 (g).

3.6 Schematic EDL structure

The EDL structure of $[N^+_{1444}][TFSA^-]$ revealed by number density and orientational distributions are summarized as a schematic image in Fig. 9. In the negative side of region III, the lying orientation of N^+_{1444} increases as the potential becomes more negative. Simultaneously, a CF_3 group in $TFSA^-$ departs from the surface of the electrode. At the II/III boundary, $TFSA^-$ completely disappears from the first ionic layer. However, at the more negative potentials in region II, N^+_{1444} still increases in the number because of the change in the orientation of N^+_{1444} from lying to standing. At the I/II boundary N^+_{1444} in the first ionic layer becomes saturated. At the more negative potentials in region I, the increase in N^+_{1444} occurs in the second ionic layer.

In the positive side of region III, $TFSA^-$ prefers the orientation in which the S_{BT}-S_{BT} vector is parallel to the electrode. The polar-part (N_{Qa}) of N^+_{1444} departs from the electrode as the potential becomes more positive. At the III/IV boundary, N^+_{1444} disappears from the first ionic layer, but a butyl chain in the N^+_{1444} remains in the first layer region. Hence, in the potentials in region IV, the accumulation of $TFSA^-$ in the first ionic layer occurs removing the butyl chain from the layer, i.e., changing in the orientation of N^+_{1444} at the second ionic layer. At more positive potentials in region V, the butyl chain completely departs from the first ionic layer, but the accumulation of $TFSA^-$ still occur with increasing potential. $TFSA^-$ presumably form a better packing structure by filling cavities between $TFSA^-$ ions and optimizing the structure of $TFSA^-$. $TFSA^-$ in the first ionic layer was not saturated within the potential region investigated in the present study.

3.7 Two Dimensional EDL structure

Since the structural changes shown above involves the change in in-plane structure of the first layer, here we analyzed two dimensional radial distribution function $g_{xy,\text{i}}$ of N_{Qa} and N_{BT} in the first layer. Fig. 10 (a) and (b) show the potential dependence of $g_{xy,\text{i}}$. Fig. 10 (c), (d), (e), (f), and (g) show snapshots of the first layer at different potentials. In the snapshot, the ions and electrode are shown as a stick except for N_{Qa} (red sphere), CB4 (green sphere), and N_{BT} (blue sphere).

First, we focus on N^+_{1444} (Fig. 10 (a)) and look at the change from positive to negative potentials. In region III, the first peak of the $g_{xy,\text{NQa}}$ appeared at $r_{xy} \sim 11$ Å at the most positive potential and shifted to the smaller r_{xy} as the potential become more negative. The peak shift means that the more $TFSA^-$ depleted from the first layer, and the more N^+_{1444} become adjacent to each other. On the other hand, in region II, the peak at $r_{xy} = 9$ Å did not show an apparent shift but became broader at the negative potentials. The broader peak indicates that N^+_{1444} in lying orientation become dominant at negative potentials, and therefore butyl groups are interposed between N_{Qa} (Fig. 10 (d)). Such butyl groups enhance the degree of freedom for the nearest neighbor distance of N_{Qa}. In addition, in region I, a new peak appeared $r_{xy} \sim 6$ Å. The new peak indicates that N_{Qa} of N^+_{1444} in standing orientation are adjacent to each other without the interposed butyl groups(Fig. 10 (c)).

Regarding $TFSA^-$, focusing on the change from negative to positive potentials, the similar tendencies were observed; the peak shift (region III) and the appearance of a new peak (Region IV). However, this new peak was not as clear as N^+_{1444} probably because the first layer was not yet saturated with $TFSA^-$ in Region IV (Fig. 10 (g)). The appearance of the clearer peak can be inferred at the more positive potentials.

The highly-ordered two-dimensional structure of ionic liquids near electrode has been proposed by MD,[45] AFM[75,76] and STM.[39] In the present study, although $g_{xy,\text{i}}$ showed neighboring distances, the high-ordered structure, such as hexagonal and linear, was not observed. Probably, the complex structure of N^+_{1444} in the first layer due to the three butyl chains does not allow such highly-ordered and well-packed structure.

3.8 Differential capacitance

Differential capacitance, C_d, of $[N^+_{1444}][TFSA^-]$ as a function of potential is shown in Fig. 11. The plots in region I and III are highlighted in blue and red for the later discussion. The error bars are the standard errors given by quadratic regression of potential-surface charge density plot (Fig. S3).

The C_d-$\Delta\phi$ plot (Fig. 11) was camel-shaped with two local maxima at ~ -0.2 and $\sim +1.1$ V. According to the mean-field lattice gas model[5] proposed by Kornyshev, in the U-shaped region between the two maxima where the electrode is moderately charged, the excluded volume effect between ions is less prominent, leading to the Gouy-Chapman model[6,7] like behavior. In contrast, the C_d decrease outside the U-shaped region reflects the excluded-volume effect between ions.

The camel shape was significantly asymmetric with respect to

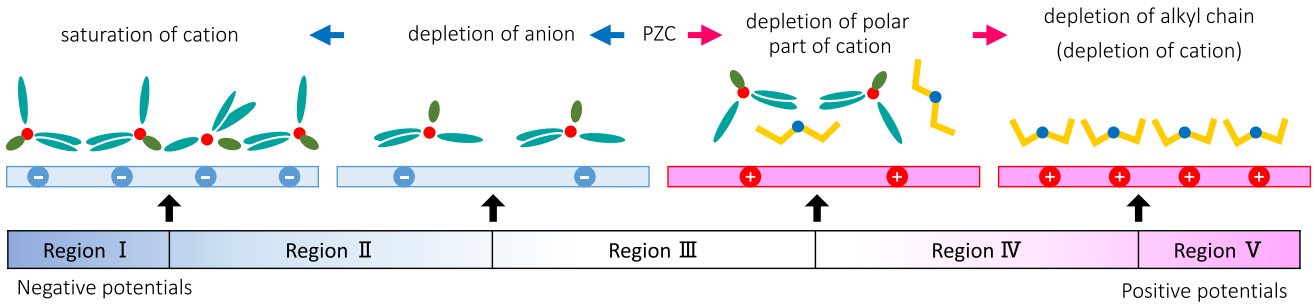

Fig. 9 Schematic illustration of the behavior of $[N^{+}_{1444}][TFSA^{-}]$ at the electric double layer.

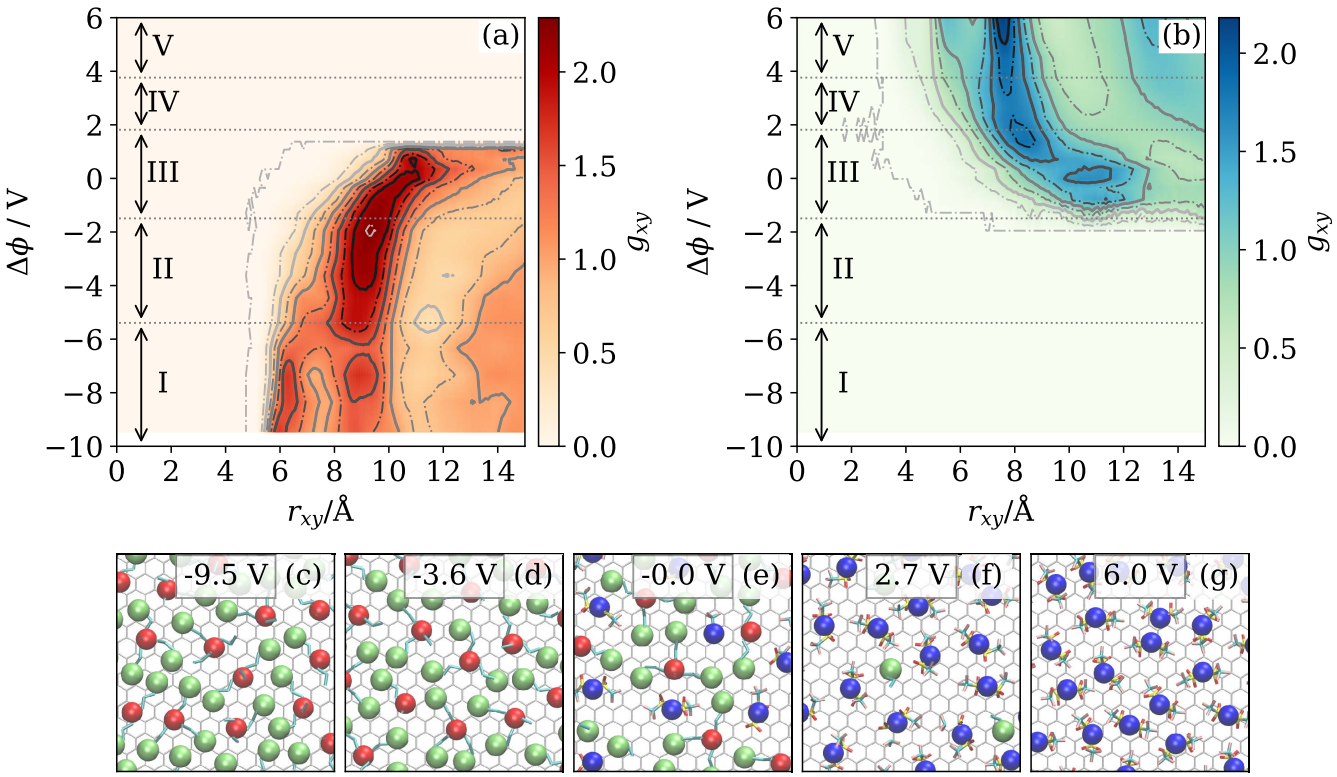

Fig. 10 (a), (b): Contour maps of two dimensional radial distribution function $g_{xy,i}(r_{xy,i})$ for N_{Qa} (a) and N_{BT} (b). The marked regions Ⅰ-Ⅴ correspond to Fig. 5. (c)-(d): Snapshots of first layer viewed from the top at different potentials. N_{Qa} (red), N_{BT} (blue), and C_{B4} (green) are highlighted as spheres.

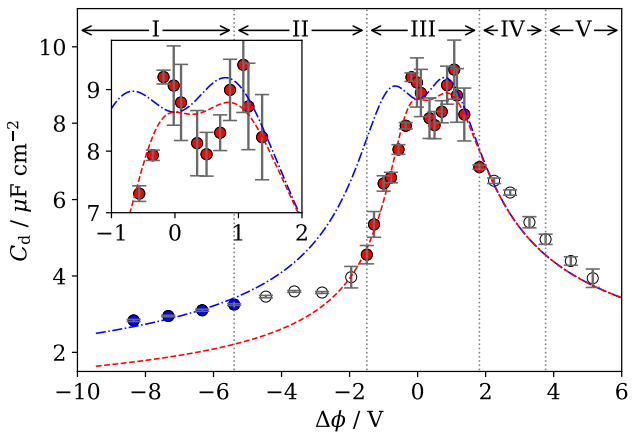

Fig. 11 C_d-$\Delta\phi$ plot. The red dashed line is the fitting curve of a theoretical equation of lattice gas model[10] by Goodwin *et al.* (eq. (7)) to the red plots. The blue dashed-dotted line is the fitting curve to the blue plots when the parameters are fixed to that of the red dashed line except for the parameter of the cation (γ_+). The marked regions I-V correspond to Fig. 5.

the local minimum at $\Delta\phi \sim 0.5$ V (see the inset in Fig. 11). Specifically, the slope at the negative potentials (-2 to 0 V) was steeper than that in the positive potentials (+1 to +4 V). Moreover, the slope at the more negative potentials (< -2 V) became constant. By the mean-field lattice gas model,[5] such kind of asymmetric $\Delta\phi$-C_d curve has been explained as a result of the difference in the size of cation and anion. Qualitatively, the model suggests that when C_d is higher at positive than at negative potentials the anion is smaller than the cation, which agrees with the DFT calculation results of the volume of N^+_{1444} and $TFSA^-$ described above.

To quantitatively analyze the C_d-$\Delta\phi$ plot, we utilized the C_d formula derived by the lattice gas model which was recently proposed by Goodwin et al.[10] In the formula, C_d is expressed as a function of potential as follows,

$$C_d = \tilde{C}_{d0}\frac{\cosh(\alpha u_0/2)}{1+2\gamma\sinh^2(\alpha u_0/2)}\sqrt{\frac{2\gamma\sinh^2(\alpha u_0/2)}{\ln(1+2\gamma\sinh^2(\alpha u_0/2))}} \quad (7)$$

where $u_0 = \frac{e\Delta\phi}{k_B T}$ is reduced potential at the electrode, $\tilde{C}_{d0}$ is C_d at PZC, α is a factor representing the short-range repulsive / attractive interactions between co-ions / counter ions, and γ is compacity, which represents the condensation capability of the ion at the EDL. γ is expressed as $\gamma = 2C_{bulk}/C_{max}$, where C_{bulk} is the concentration of ions in bulk and C_{max} is the maximum concentration of ions at EDL. For the case of the present study, different γ values of N^+_{1444} and $TFSA^-$ (γ_+ and γ_-) should be defined because they have different C_{max}. The γ values are approximately expressed[5] as a function of u_0 as follows,

$$\gamma = \gamma_- + \frac{\gamma_+ - \gamma_-}{1+\exp(\alpha u_0).} \quad (8)$$

We fitted the formula to the C_d-$\Delta\phi$ plot of $[N^+_{1444}][TFSA^-]$ obtained in the present study. The fitting parameters are $\tilde{C}_{d0}, \alpha, \gamma_+$, and γ_-. The best fit parameters are listed in Table 1.

The curve fitted for all plots is shown in Fig. S6. As Fig. S6 shows, the lattice gas model reproduced the C_d for the regions III, IV, and V, although it could not reproduce that for the regions I and II. It is inadequate to discuss the theoretical curve given by the fitting including the plots beyond the model. Hence, we limited the fitting region to the region III. This fitted curve is shown as a red dashed line in Fig. 11. The newly fitted curve was similar to the old curve (see Fig. S6 to compare them).

For C_d-$\Delta\phi$ plot compared with the fitted curve, there are the small discrepancies at positive potentials and large discrepancy at negative potentials. The former implies that the replacement of $TFSA^-$ with N^+_{1444} can basically be interpreted within the lattice gas model. The latter large discrepancy indicates that there is also a discrepancy in the behaviors of ions between the lattice gas model and N^+_{1444} in region I and II where $TFSA^-$ is depleted at the first layer. The most likely reason is the change in orientational preference of N^+_{1444} from lying to standing as the potential becomes more negative in region II (Fig. 7), because the lattice gas model does not consider orientational effect explicitly. A N^+_{1444} in the standing orientation occupies a significantly smaller area on the electrode than that in the lying orientation. Therefore the increase in the fraction of standing orientation causes the increase in the C_{max} of N^+_{1444}. In the representation of the lattice gas model, $[N^+_{1444}][TFSA^-]$ should have smaller γ_+ at highly negative potentials compared with the apparent γ_+ around PZC.

To test the idea, we fixed the parameters ($\tilde{C}_{d0}$, α, γ_-) other than γ_+, and fitted the formula to the plots in region I. As a result, the fitted curve (blue dashed-dotted line) reproduced the plots in region I, indicating that the orientational effect on C_{max} has an important role to the $\Delta\phi$-C_d curve. Describing explicit orientational effect is a possible extension of the lattice gas model. In a simple way, this may be done by modifying eq. 8 to describe decrease in γ at negative potentials.

Comparison of the present simulation results with experimental ones would be worthful. First of all, in our previous zero-frequency C_d measurement using the electrocapillarity,[21] the value of γ_- in 1-ethyl-3-methylimidazolium (C^+_{2mim}) $TFSA^-$ was found to be 0.5 by fitting using a lattice gas model,[8] whereas the γ_- value for $TFSA^-$ (~ 0.2) in the present study is significantly smaller. According to the lattice gas model,[5] γ ($= 2C_{bulk}/C_{max}$) of an ion is not specific to the ion but depends on the counter ion because the latter affects C_{bulk}. The larger size of N^+_{1444} than C^+_{2mim} leads to the smaller C_{bulk} and then smaller γ_- in $[N^+_{1444}][TFSA^-]$ than $[C^+_{2mim}][TFSA^-]$. On the other hand, the entire C_d values are significantly smaller than the experimental values, even taking into account differences between QaILs and imidazolium-based ILs. The difference between potentials at the two maxima of the camel shape are larger than that in 1-octyl-3-methylimidazolium BF_4^-.[20] To obtain further information on the discrepancies the comparison would be helpful with experimental zero-frequency C_d of $[N^+_{1444}][TFSA^-]$ by using the pendant drop method[20,21]. The measurement and the analysis are in progress in our laboratory.

4 Conclusions

Focusing on N^+_{1444}, which is a quaternary-ammonium cation having three long-chain alkyl groups, we clarified the potential de-

Table 1 Best fit parameters of the fitting using theoretical equation of lattice gas model[10] by Goodwin *et al.*

range of $\Delta\phi$ for fitting / V	C_0 / μFcm^{-2}	γ_+	γ_-	α
−8.3 to 5.1 (whole range)	8.6 ± 0.3	0.56 ± 0.09	0.24 ± 0.03	0.09 ± 0.01
−1.5 to 1.8	8.6 ± 0.2	0.6 ± 0.1	0.23 ± 0.02	0.09 ± 0.01
−8.3 to −5.4	8.6 (fixed)	0.26 ± 0.01	0.23 (fixed)	0.09 (fixed)

pendence of the electric double layer structure and differential capacitance at the interface between $[N^+_{1444}][TFSA^-]$ and graphene electrode. The composition of the first layer was evaluated based on the surface density of the polar parts of N^+_{1444} and $TFSA^-$, and the butyl group in N^+_{1444}. From the first layer composition, the potential was found to be divided into five regions. In particular, at negative potentials, the number of polar parts of N^+_{1444} increased as the potential became negative even at the potentials where the butyl group saturated in the first layer (region II).

Orientational analysis of the butyl group in the first layer revealed that N^+_{1444} has the orientational change from lying to standing as the potential becomes negative in the region II. Standing orientation is not entropically favored because it reduces the entropic gain originating from the translational movement of ions in the IL bulk. Therefore, the standing orientation became competitive only in the positive and negative potential regions where the electrostatic energy between ions and electrode is large.

The C_d-$\Delta\phi$ plot was camel-shaped, and its behavior around $\Delta\phi$ = 0 V was reproduced by fitting the theoretical formula of the lattice gas model. However, C_d had a discrepancy between the fitting curve and the MD values at potentials in region II and at the more negative potentials. The discrepancy is correlated with the change in orientation of N^+_{1444}. The decrease in C_d at negative potentials is likely to be alleviated by the change in orientation of N^+_{1444}.

Conflicts of interest

There are no conflicts to declare.

Acknowledgements

This work was partly supported by JSPS KAKENHI (No. 18K05171), TEPCO Memorial Foundation, and Kato Foundation for Promotion of Science.

References

1 A. Lewandowski and A. Swiderska-Mocek, *J. Power Sources*, 2009, **194**, 601–609.
2 M. P. S. Mousavi, B. E. Wilson, S. Kashefolgheta, E. L. Anderson, S. He, P. Bühlmann and A. Stein, *ACS Appl. Mater. Interfaces*, 2016, **8**, 3396–3406.
3 S. Y. Lee, A. Ogawa, M. Kanno, H. Nakamoto, T. Yasuda and M. Watanabe, *J. Am. Chem. Soc.*, 2010, **132**, 9764–9773.
4 M. Armand, F. Endres, D. R. MacFarlane, H. Ohno and B. Scrosati, *Nat. Mater*, 2009, **8**, 621–629.
5 A. A. Kornyshev, *J. Phys. Chem. B*, 2007, **111**, 5545–5557.
6 D. L. Chapman, *Phil. Mag.*, 1913, **25**, 475–481.
7 M. Gouy, *J. Phys. Theor. Appl.*, 1910, **9**, 457–468.
8 Y. Han, S. Huang and T. Yan, *J. Phys. Condens. Matter*, 2014, **26**, 284103.
9 A. C. Maggs and R. Podgornik, *Soft Matter*, 2016, **12**, 1219–1229.
10 Z. A. H. Goodwin, G. Feng and A. A. Kornyshev, *Electrochim. Acta*, 2017, **225**, 190–197.
11 R. Downing, B. K. Berntson, G. V. Bossa and S. May, *J. Chem. Phys.*, 2018, **149**, 204703.
12 J. Vatamanu, O. Borodin and G. D. Smith, *J. Am. Chem. Soc.*, 2010, **132**, 14825–14833.
13 J. Vatamanu, O. Borodin, D. Bedrov and G. D. Smith, *J. Phys. Chem. C*, 2012, **116**, 7940–7951.
14 Z. Z. Hu, J. Vatamanu, O. Borodin and D. Bedrov, *Electrochim. Acta*, 2014, **145**, 40–52.
15 J. B. Haskins and J. W. Lawson, *J. Chem. Phys.*, 2016, **144**, 184707.
16 M. M. Islam, M. T. Alam and T. Ohsaka, *J. Phys. Chem. C*, 2008, **112**, 16568–16574.
17 V. Lockett, R. Sedev, J. Ralston, M. Horne and T. Rodopoulos, *J. Phys. Chem. C*, 2008, **112**, 7486–7495.
18 B. Roling, M. Druschler and B. Huber, *Faraday Discuss.*, 2012, **154**, 303–311.
19 T. Jansch, J. Wallauer and B. Roling, *J. Phys. Chem. C*, 2015, **119**, 4620–4626.
20 N. Nishi, A. Hashimoto, E. Minami and T. Sakka, *Phys. Chem. Chem. Phys.*, 2015, **17**, 5219–5226.
21 N. Nishi, S. Yasui, A. Hashimoto and T. Sakka, *J. Electroanal. Chem.*, 2017, **789**, 108–113.
22 N. Nishi, Y. Kojima, S. Katakura and T. Sakka, *Electrochemistry*, 2018, **86**, 38–41.
23 K. Motobayashi, K. Minami, N. Nishi, T. Sakka and M. Osawa, *J. Phys. Chem. Lett.*, 2013, **4**, 3110–3114.
24 K. Motobayashi, N. Nishi, Y. Inoue, K. Minami, T. Sakka and M. Osawa, *J. Electroanal. Chem.*, 2017, **800**, 126–133.
25 A. Uysal, H. Zhou, G. Feng, S. S. Lee, S. Li, P. Fenter, P. T. Cummings, P. F. Fulvio, S. Dai, J. K. McDonough and Y. Gogotsi, *J. Phys. Chem. C*, 2014, **118**, 569–574.
26 S. Makino, Y. Kitazumi, N. Nishi and T. Kakiuchi, *Electrochem. Commun.*, 2011, **13**, 1365–1368.
27 N. Nishi, Y. Hirano, T. Motokawa and T. Kakiuchi, *Phys. Chem. Chem. Phys.*, 2013, **15**, 11615–11619.
28 A. Uysal, H. Zhou, G. Feng, S. S. Lee, S. Li, P. T. Cummings, P. F. Fulvio, S. Dai, J. K. McDonough, Y. Gogotsi and P. Fenter, *J. Phys. Condens. Matter*, 2015, **27**, 032101.
29 M. Mezger, H. Schröder, H. Reichert, S. Schramm, J. S. Okasinski, S. Schröder, V. Honkimäki, M. Deutsch, B. M. Ocko, J. Ralston, M. Rohwerder, M. Stratmann and H. Dosch, *Science*, 2008, **322**, 424–428.
30 H. Zhou, M. Rouha, G. Feng, S. S. Lee, H. Docherty, P. Fenter,

P. T. Cummings, P. F. Fulvio, S. Dai, J. McDonough, V. Presser and Y. Gogotsi, *ACS Nano*, 2012, **6**, 9818–9827.
31 N. Nishi, T. Uruga and H. Tanida, *J. Electroanal. Chem.*, 2015, **759**, 129–136.
32 M. Chu, M. Miller and P. Dutta, *ACS Cent. Sci.*, 2016, **2**, 175–180.
33 P. Reichert, K. S. Kjaer, T. Brandt van Driel, J. Mars, J. W. Ochsmann, D. Pontoni, M. Deutsch, M. M. Nielsen and M. Mezger, *Faraday Discuss.*, 2017, **206**, 141–157.
34 Y. Lauw, M. D. Horne, T. Rodopoulos, V. Lockett, B. Akgun, W. A. Hamilton and A. R. Nelson, *Langmuir*, 2012, **28**, 7374–7381.
35 N. Nishi, J. Uchiyashiki, Y. Ikeda, S. Katakura, T. Oda, M. Hino and N. L. Yamada, *J. Phys. Chem. C*, 2019, **123**, 9223–9230.
36 R. Atkin and G. G. Warr, *J. Phys. Chem. C*, 2007, **111**, 5162–5168.
37 F. Endres, N. Borisenko, S. Z. El Abedin, R. Hayes and R. Atkin, *Faraday Discuss.*, 2012, **154**, 221–233.
38 S. Perkin, *Phys. Chem. Chem. Phys.*, 2012, **14**, 5052–5062.
39 Y. Z. Su, Y. C. Fu, J. W. Yan, Z. B. Chen and B. W. Mao, *Angew. Chem. Int. Ed.*, 2009, **48**, 5148–5151.
40 S. Baldelli, *Acc. Chem. Res.*, 2008, **41**, 421–431.
41 S. Y. Xu, S. R. Xing, S. S. Pei, V. Ivaništšev, R. Lynden-Bell and S. Baldelli, *J. Phys. Chem. C*, 2015, **119**, 26009–26019.
42 S. G. Harroun, T. J. Abraham, C. Prudhoe, Y. Zhang, P. J. Scammells, C. L. Brosseau, C. C. Pye and R. D. Singer, *Phys. Chem. Chem. Phys.*, 2013, **15**, 19205–19212.
43 J. C. Rubim, F. A. Trindade, M. A. Gelesky, R. F. Aroca and J. Dupont, *J. Phys. Chem. C*, 2008, **112**, 19670–19675.
44 V. Ivaništšev and M. V. Fedorov, *Electrochem. Soc. Interface*, 2014, **23**, 65–69.
45 S. A. Kislenko, I. S. Samoylov and R. H. Amirov, *Phys. Chem. Chem. Phys.*, 2009, **11**, 5584–5590.
46 R. M. Lynden-Bell, A. I. Frolov and M. V. Fedorov, *Phys. Chem. Chem. Phys.*, 2012, **14**, 2693–2701.
47 S. Sharma and H. K. Kashyap, *J. Phys. Chem. C*, 2015, **119**, 23955–23967.
48 S. Sharma and H. K. Kashyap, *J. Phys. Chem. C*, 2017, **121**, 13202–13210.
49 S. Sharma, H. S. Dhattarwal and H. K. Kashyap, *J. Mol. Liq.*, 2019, **291**, 111269.
50 N. Nishi, K. Minami, K. Motobayashi, M. Osawa and T. Sakka, *J. Phys. Chem. C*, 2017, **121**, 1658–1666.
51 N. Nishi, Y. Ikeda and T. Sakka, *J. Electroanal. Chem.*, 2018, **817**, 210–216.
52 N. Nishi, Y. Yasui, T. Uruga, H. Tanida, T. Yamada, S. Nakayama, H. Matsuoka and T. Kakiuchi, *J. Chem. Phys.*, 2010, **132**, 164705.
53 N. Nishi, T. Uruga, H. Tanida and T. Kakiuchi, *Langmuir*, 2011, **27**, 7531–7536.
54 S. Katakura, N. Nishi, K. Kobayashi, K.-i. Amano and T. Sakka, *J. Phys. Chem. C*, 2019, **123**, 7246–7258.
55 W. Smith and T. R. Forester, *J. Mol. Graph.*, 1996, **14**, 136–141.
56 J. N. Canongia Lopes and A. A. H. Pádua, *J. Phys. Chem. B*, 2004, **108**, 16893–16898.
57 W. L. Jorgensen, D. S. Maxwell and J. TiradoRives, *J. Am. Chem. Soc.*, 1996, **118**, 11225–11236.
58 U. Essmann, L. Perera, M. L. Berkowitz, T. Darden, H. Lee and L. G. Pedersen, *J. Chem. Phys.*, 1995, **103**, 8577–8593.
59 I. Leontyev and A. Stuchebrukhov, *Phys. Chem. Chem. Phys.*, 2011, **13**, 2613–26.
60 C. Schröder, *Phys. Chem. Chem. Phys.*, 2012, **14**, 3089–102.
61 V. Chaban, *Phys. Chem. Chem. Phys.*, 2011, **13**, 16055–16062.
62 H. J. C. Berendsen, J. P. M. Postma, W. F. van Gunsteren, A. DiNola and J. R. Haak, *J. Chem. Phys.*, 1984, **81**, 3684–3690.
63 S. C. Harvey, R. K. Z. Tan and T. E. Cheatham Iii, *J. Comput. Chem.*, 1998, **19**, 726–740.
64 S. Nose, *Mol. Phys.*, 1984, **52**, 255–268.
65 W. G. Hoover, *Phys. Rev. A. Gen. Phys.*, 1985, **31**, 1695–1697.
66 G. Bussi, D. Donadio and M. Parrinello, *J. Chem. Phys.*, 2007, **126**, 014101.
67 K. I. Amano, Y. Yokota, T. Ichii, N. Yoshida, N. Nishi, S. Katakura, A. Imanishi, K. I. Fukui and T. Sakka, *Phys. Chem. Chem. Phys.*, 2017, **19**, 30504–30512.
68 K. Amano, T. Hayashi, K. Hashimoto, N. Nishi and T. Sakka, *Journal of Molecular Liquids*, 2018, **257**, 121–131.
69 V. Ivaništšev, K. Kirchner, T. Kirchner and M. V. Fedorov, *J. Phys. Condens. Matter*, 2015, **27**, 102101.
70 M. Z. Bazant, B. D. Storey and A. A. Kornyshev, *Phys. Rev. Lett.*, 2011, **106**, 046102.
71 M. J. Frisch, G. W. Trucks, H. B. Schlegel, G. E. Scuseria, M. A. Robb, J. R. Cheeseman, G. Scalmani, V. Barone, B. Mennucci, G. A. Petersson, H. Nakatsuji, M. Caricato, X. Li, H. P. Hratchian, A. F. Izmaylov, J. Bloino, G. Zheng, J. L. Sonnenberg, M. Hada, M. Ehara, K. Toyota, R. Fukuda, J. Hasegawa, M. Ishida, T. Nakajima, Y. Honda, O. Kitao, H. Nakai, T. Vreven, J. A. Montgomery, J. E. Peralta, F. Ogliaro, M. Bearpark, J. J. Heyd, E. Brothers, K. N. Kudin, V. N. Staroverov, R. Kobayashi, J. Normand, K. Raghavachari, A. Rendell, J. C. Burant, S. S. Iyengar, J. Tomasi, M. Cossi, N. Rega, J. M. Millam, M. Klene, J. E. Knox, J. B. Cross, V. Bakken, C. Adamo, J. Jaramillo, R. Gomperts, R. E. Stratmann, O. Yazyev, A. J. Austin, R. Cammi, C. Pomelli, J. W. Ochterski, R. L. Martin, K. Morokuma, V. G. Zakrzewski, G. A. Voth, P. Salvador, J. J. Dannenberg, S. Dapprich, A. D. Daniels, Farkas, J. B. Foresman, J. V. Ortiz, J. Cioslowski and D. J. Fox, *Gaussian 09, Revision B.01*, 2009.
72 F. Oosawa and S. Asakura, *J. Chem. Phys.*, 1954, **22**, 1255–1256.
73 M. Kinoshita, *Chemical Engineering Science*, 2006, **61**, 2150–2160.
74 R. Fantoni and A. Santos, *Phys. Rev. E*, 2013, **87**, 042102.
75 A. Elbourne, S. McDonald, K. Voichovsky, F. Endres, G. G. Warr and R. Atkin, *ACS Nano*, 2015, **9**, 7608–7620.
76 W. Y. Tsai, J. Come, W. Zhao, R. X. Wang, G. Feng, B. P. Thapaliya, S. Dai, L. Collins and N. Balke, *Nano Energy*, 2019, **60**,

886–893.